universität wien

MASTERARBEIT / MASTER'S THESIS

Titel der Masterarbeit / Title of the Master's Thesis

„Rock deformation record in (and around) boudinaged dykes–high finite strain examples from Spitz (Austria)"

verfasst von / submitted by

Stephan Höpfl, BSc

angestrebter akademischer Grad / in partial fulfilment of the requirements for the degree of

Master of Science (MSc)

Wien, 2019 / Vienna 2019

Studienkennzahl lt. Studienblatt / degree programme code as it appears on the student record sheet:	A 066 815
Studienrichtung lt. Studienblatt / degree programme as it appears on the student record sheet:	Masterstudium Erdwissenschaften UG2002
Betreut von / Supervisor:	Dr. Anna Rogowitz, MSc
Mitbetreut von / Co-Supervisor:	

Table of Contents

Abstract

Analog and numerical models of the progressive evolution of boudinage have shown that the main factors controlling the development and final shape of boudins are the flow regime, orientation and spacing of the inter-boudin surface, viscosity contrast and the layer orientation and thickness. Variation of these parameters can cause complex behavior of boudin separation and rotation of the boudin segments inducing complex perturbation strain in the host rocks.
The former quarry Fehringer nearby Spitz an der Donau (Austria) represents an excellent natural laboratory to study the influence of the geometry of interboudin surfaces, viscosity contrast and layer thickness on boudin evolution at high finite strain. The exposed boudin structures vary extremely in their macroscopical appearance indicating the activity of different deformation mechanisms. Investigating the macro- and microstructures of these boudin structures might help to increase the knowledge of processes resulting in such boudin types.

Geologically the exposed rocks belong to the central European Variscan orogeny. They include amphibolites, quartzites, paragneiss, schists and marbles of which the latter represents the main unit within the quarry. The highly deformed rocks have experienced metamorphic conditions of around 700-800 °C at 8 kbar and have been syntectonically intruded by pegmatitic and aplitic dykes. During continuous top-to-the SE shearing, dykes have been rotated into the shear direction resulting in stretching, boudinage and rotation of boudin segments. The observed boudins preserve various shapes including pinch-and-swell, splayed, but also blocky geometries suggesting a progressively changing viscosity contrast possibly resulting from local metamorphic or chemical induced rheological weakening or cooling.
Using space for time, the changing deformation mechanisms and flow patterns are characterized for the host rock marbles and the aplitic dykes.
Based on the great variety of boudin types found at the outcrop, it was decided to compare two different boudin End-Members (1) Blocky-Domino Boudin and (2) Pinch-and-Swell/Tapered Boudin, to deduct common or discerning processes that would allow for a better understanding of these structures.
In both types, the grain size of the marble host rock is decreasing with increasing proximity to the aplitic dyke, accompanied by a more distinct shape preferred orientation (SPO) of the calcite grains, both likely due to a localization of deformation around the aplite.
Intracrystalline distortion has been analyzed via electron backscatter diffraction (EBSD) mapping allowing for a quantification of the misorientation in different localities throughout these samples. EBSD analysis revealed increased crystal plasticity, either within calcite grains located at the aplite-host rock boundary or in quartz grains within the aplite center depending on boudin type. In general all aplite dykes are surrounded by a metasomatic halo of diopside. Only where late cracks occur this halo is missing, instead we observe precipitations of quartz and less common calcite.

Geodynamically, it stands to reason that after the intrusion of the dykes they were later rotated and/or boudinaged mainly depending on their orientation and aspect ratio. The occurrence of both compressional and extensional structures, which can be observed in a multitude of samples, might be due the rotation of dykes into the fields of instantaneous stretching/shortening and the consequential varying behavior of these dykes. Certain samples also show signs of high shear strains (γ = >20) and point towards successive deformational episodes.

Zusammenfassung

Sowohl analoge- als auch numerische Modelle zur progressiven Entwicklung von Boudinage zeigten, dass die wichtigsten Faktoren zur Kontrolle der Entwicklung und endgültigen Form von Boudins, das Fließregime, die Orientierung, die Breite der Inter-Boudin Flächen, der Viskositätskontrast und die Orientierung der Lage sowie deren Mächtigkeit seien. Eine Veränderung dieser Werte ist in der Lage eine drastische Erhöhung der Rotation und Separation der Boudin-Segmente vorherzurufen, wobei beides zu einer komplexen Verformung des Wirtsgesteins führen kann.

Der ehemalige Steinbruch Fehringer bei Spitz an der Donau, Österreich stellt eine hervorragende natürliche Lokalität zur Untersuchung des Einflusses der Geometrie von Inter-Boudin Flächen, Viskositätskontrast und Lagenmächtigkeit auf die Entwickliung von Boudins unter hoher finiter Verformung dar. Dieser Zusammenhang und das generelle Interesse an der Analyse der zugehörigen Mikrostrukturen repräsentiert die Hauptmotivation für dieses Projekt. Eine makroskopische sowie submakroskopische Analyse dieser Strukturen könnte zum Verstehen der aktiven Mechanismen beitragen und somit unser generelles Verständnis dieser Prozesse erweitern.

Regionalgeologisch sind die aufgeschlossenen Gesteine dem zentralen europäischen Variszikum zuzuordnen. Dazu zählen Amphibolite, Quartzite, Paragneisse, Schiefer und Marmore, wobei der Steinbruch Fehringer hauptsächlich aus letzterem besteht. Die stark deformierten Gesteine wurden unter 700-800 °C und 8 kbar metamorph umgewandelt und syntektonisch von Aplit- und Pegmatitgängen intrudiert. Während der kontinuierlichen top-to the SE Scherung wurden die intrudierten Gänge in die Scherrichtung rotiert, was zur Streckung, Boudinage und Rotation dieser Boudin-Segmente führte. Die auftretenden Boudin-Typen reichen von „pinch-and-swell“ Strukturen bis zu „tapered“ boudins und blockigen Geometrien, welches eine progressive Änderung des Viskositätskontrast suggeriert, möglicherweise resultierend aus chemisch oder lokal metamorph bedingten rheologischen Änderungen oder Abkühlung.

Unter Betrachtung von Raum und Zeit werden die variierenden Deformationsmechanismen und Fließmuster sowohl für das Wirtsgestein als auch für die intrudierten Ganggesteine charakterisiert.

Aufgrund der hohen Vielfalt an Boudin-Klassen wurden zwei sich gegenüberliegende Haupttypen, (1) blockige Domino-Boudins und (2) pinch-and-swell/tapered Boudins,

miteinander verglichen um entweder typische oder ungewöhnliche Prozesse festzuhalten die zu einem besseren Verständnis dieser Strukturen führen würden. Beide Typen weisen eine Eniedrigung der Korngröße des Marmors mit abnehmender Distanz zum Übergang des Aplits auf, welche mit einer deutlicheren Formvorzugsregelung der Kalzitkörner einhergeht, höchstwahrscheinlcih aufgrund einer Lokalisation von Deformation um den Aplit.
Durch die Analyse der intrakristallinen Deformation über Elektronenrückstreubeugung (EBSD) konnte eine Quantifizierung der Misorientierung in unterschiedlichen Lokalitäten der Proben gemessen werden. Diese Untersuchungen zeigten, abhängig von Boudin-Klasse, entweder am Übergang zwischen dem Marmor und dem Aplit, oder auch in den Quarzkörnern innerhalb des Aplits teils hohe Mengen an Kristallplastizität auf. Zudem sind annähernd alle Aplitgänge von einem metasomatischen Saum aus Diopsid umgeben. Nur jüngere Brüche zeigen diesen Saum nicht, stattdessen treten dort häufig Ausfällungen von Quarz und, weniger häufig, Kalzit auf.

Geodynamisch betrachtet, scheint es wahrscheinlich, dass nach der Intrusion der Gänge selbige hautpsächlich aufgrund ihrer Orientierung und ihres Achsenverhätnisses rotiert und boudiniert wurden. Das Auftreten von sowohl kompressiven als auch extensiven Strukturen, welche in einer Vielzahl von Proben betrachtet werden können, könnte auf ein Rotieren der Gänge in unterschiedliche Quadranten der Dehnung/Verkürzung und das daraus folgende variierende Verhalten der Gänge zurückzuführen sein. Bestimmte Proben zeigen auch Anzeichen von hoher Scherverformung (γ => 20) und weisen auf aufeinanderfolgende Deformationsepisoden hin.

Introduction

Boudinage is a geological phenomenon that was firstly documented by Ramsay (1881) and named and described by Lohest (1909) as a fractured sheet of rock situated between nonfractured schistose or gneissic rocks. Later in 1955 Ramberg released an influential paper in which these structures were described in more detail and classified according to their geometry. Back then, Ramberg (1955) documented multiple boudin-types based on their shape and geometry and elaborated on how they are formed and which processes were active. This first classification included the following types: (1) rectangular bodies with sharp corners indicating that they behaved brittle and strong relative to the adjacent rocks, (2) Barrel-Shaped boudins caused by plastic flowage, (3) Lens-Shaped boudins representing a more extensive version of (2) and (4) lenticular boudins.

A contemporary, more complete nomenclature by Goscombe et al. (2004) has a kinematic approach, consisting of three classes: (1) symmetrical no-slip (2) asymmetrical S-slip (3) asymmetrical A-Slip (Goscombe et al., 2004). In addition, it features five End-Member boudin block geometries named drawn, torn, domino, gash and shearband boudins (Fig. 1). Extensive studies of boudin structures over the last decades by the means of analog modeling (Kidan and Cosgrove, 1996; Mandal et al., 2007; Marques et al., 2012; Carreras et al., 2013 and numerical modeling (Schmalholz et al., 2008; Iyer and Podladchikov, 2009; Schöpfer et al., 2011), investigating the complex behavior of boudin structures, have shown how versatile boudinage structures can become.

Kidan and Cosgrove (1996) conducted experiments along multilayers made of Plasticine and Paraffin wax. One of their main conclusions showed that although the structures formed by layer parallel and layer normal compression are the result of the same basic instability, layer normal compression structures like pinch-and-swell structures are much harder to generate. Additionally, their growth rate is considerably lower compared to layer parallel compression structures. Mandal et al. (2007) attempted to use rigid boudinaged objects as strain gauges and discovered that extensional strain determined from boudinage structures is less than the actual bulk strain and that for any type of boudin structure the difference between boudinage strain and bulk extension is greater at simple shear conditions compared to pure shear environments.

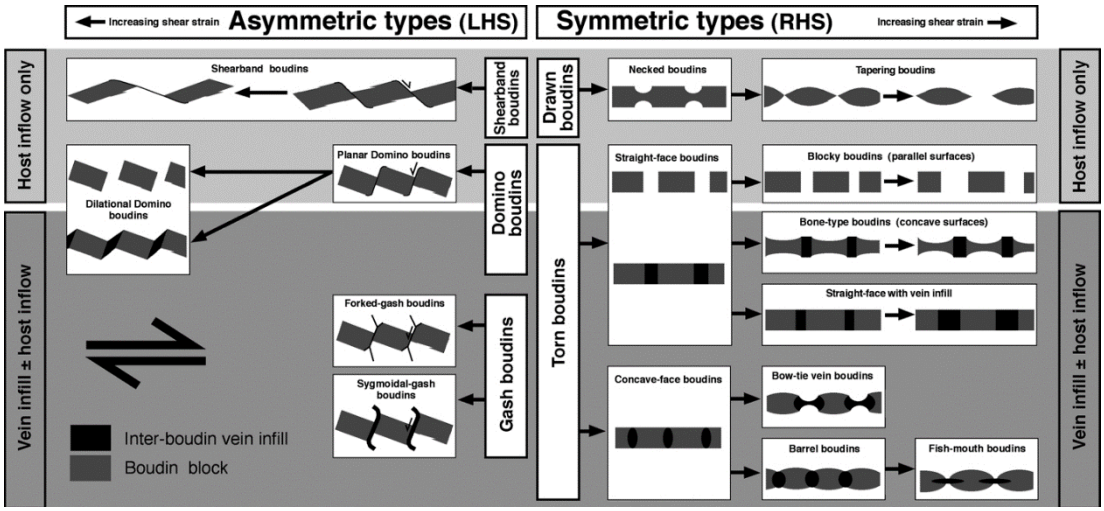

Fig. 1 Overview of different types of Boudins as a result of the varying criteria in effect (from. Goscombe et al., 2004, Fig. 3)

The five End-Member boudin types established by Goscombe et al., (2004) can be attributed as groups to the kinematic classes, whereas drawn and torn boudins extend by no-slip (class 1), domino and gash boudins by A-slip (class 2) and shearbands are the result of S-Slip boudinage (class 3). Over the last decades various numerical, analogue and field based studies have studied possible factors resulting in different boudin geometries (Goldstein, 1988; Jordan, 1991; Swanson, 1992; Grasemann and Stüwe, 2001; Passchier and Druguet, 2002; Goscombe et al., 2004; Mandal et al., 2007) showing that the initial fracture geometry, the orientation of the boudinaged layer, the width of the inter boudin zone, the competence contrast, the type of background deformation and the finite amount of strain (Fig. 2) are some of the key factors influencing the finite boudin geometry.

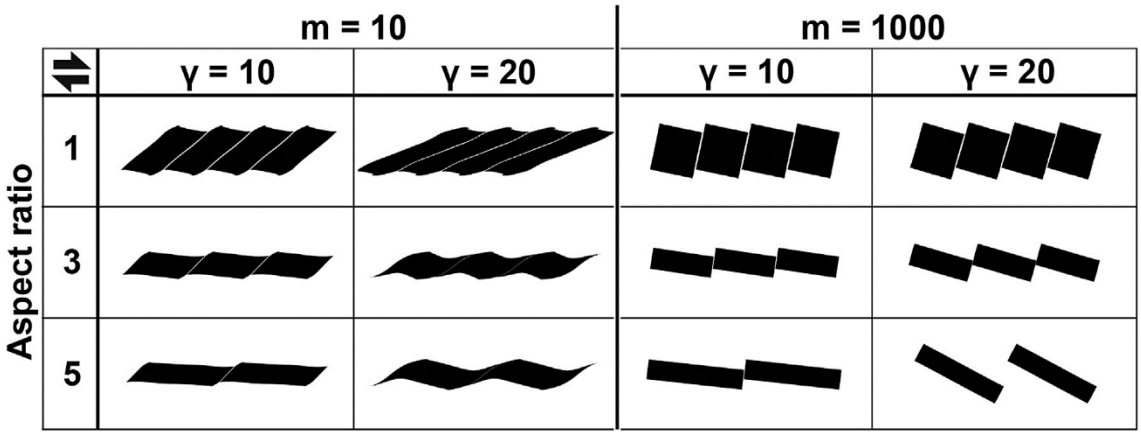

Fig. 2 The effect of three different factors (AR, m=viscosity, γ=shear strain) on varying boudin assemblages with a gap width of 0.05 (from Dabrowski and Grasemann, 2014, Fig. 2)

In this study I focus on structures occurring on a microscale in order to analyze active deformation mechanisms within boudin segments and their surrounding matrix during boudinization. The investigated boudin structures are located in Spitz an der Donau, SW of

Vienna, at a former marble quarry named Fehringer, which has been affected by rockfalls since the 1960s due to improper excavation and precipitation. It features a high variety of boudin geometries, needing for a detailed classification to make assumptions on the flow regime and to receive an idea of the structural-tectonic environment in which the boudins were formed.

Two Types of Boudin End-Members were established and analysed using an identic workflow for the purpose of comparison. A detailed characterization of the microfabric by optical and secondary electron microscopy (SEM) including electron backscatter diffraction (EBSD) mapping help to gain a better understanding of the mechanical and chemical feedback processes at lower crustal conditions.

Geological Setting

Moldanubian

The former quarry Fehringer belongs to the Drosendorfer Nappe system which is part of the central European Variscan orogeny. Together with the Ostrong- and the Gföhl Nappe system it forms the Moldanubian (Fig. 3), one main part of the Bohemian Massif (Racek et al., 2006; Racek et al., 2017). The Drosendorfer Nappe or "Bunte Serie/Varied Group" is characterized by its great variety of rocks including, amphibolites, quartzites, paragneisses, schists and marbles of which the latter represent the main unit within the quarry (Linner 1996; Racek et al., 2006; Racek et al., 2017). The highly deformed rocks have experienced metamorphic conditions of around 700-800 °C at 7-11 kbar and have been syntectonically intruded by pegmatitic and aplitic dykes (Petrakakis, 1997; Kolenovská et al., 1999; Štípská and Powell 2005a; Racek et al., 2006; Racek et al., 2017).
The Gföhl unit comprises migmatitic orthogneisses and felsic granulites with mostly magmatic protoliths, containing subordinate mafic and ultramafic rocks (Fiala et al., 1987; Janoušek et al., 2004; Hasalová et al., 2008 a, b, c;). Its original material originates from the lower orogenic crust and has experienced metamorphic conditions of 800-900 °C and 18-20 kbar (Medaris et al., 1995; Cooke 2000; Štípská and Powell 2005a, Tajčmanová et al., 2006, Racek et al., 2008;, b; Nahodilová et al., 2014; Racek et al., 2017). Finally, the Ostrong unit, also known as "Monotone Serie/Monotonous Group" mainly consists of paragneisses but likewise comprises, calc-silicate and mafic rocks as well as small amounts of quartzite (Kröner et al., 1988). These migmatitic paragneisses contain big amounts of cordierite but show no signs of garnet, which is indicative for temperatures not higher than 750 °C and 4-6 kbar (Linner, 1996). However, granulite facies overprinted eclogites also provide evidence for a high temperature-mid pressure event in certain areas of the Ostrong-unit (O' Brien, 1997).

The entire Moldanubian displays a heavy metamorphic overprint at temperatures of around 700 °C and 4-8 kbar (Racek et al., 2006; Tajčmanová et al., 2006; Štípská et al., 2008; Racek et al., 2017). Structurally, the Moldanubian represents a nappe stack of three main units with the Gföhl unit forming the top (Fuchs, 1976; Thiele, 1976). It was thrusted over the bottom Ostrong unit and the middle Drosendorf unit and finally over the Brunia microcontinent (Fuchs, 1976; Thiele, 1976) or Brunovistulian continental block (Dudek, 1980). This final thrusting event sometimes serves as an explanation for the uniform, metamorphic Moldanubian overprint mentioned further above (Petrakakis, 1997 and references therein). Various studies state that the metamorphic peak of the Moldanubian happened during the Carbon (Kröner et al., 2000a; Friedl et al., 2003, and references therein). However, further information points towards additional magmatic events whilst the Ordovician, Silurian and Devonian.

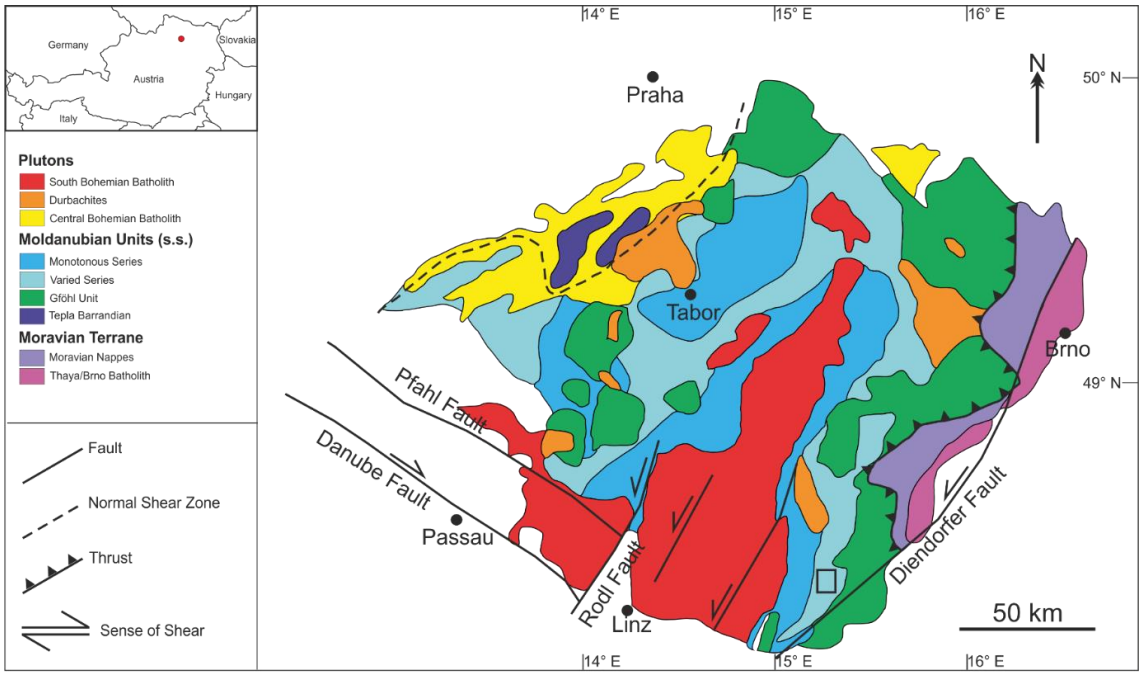

Fig. 3 Geological Map of the Moldanubian part of the Bohemian Massive; the outlined rectangle marks the position of the investigated outcrop (modified after Zeitlhofer et al., 2014, Fig. 1)

Quarry Fehringer

The former quarry Fehringer was active until 1961, when a mass movement of 70.000 m^3 interrupted further exploitation. The mass movement was mainly caused by the excessive excavation of the quarry and was later on followed by additional landslides, some caused by precipitation. These mass movements were mainly concentrated on the SW-part of the quarry, which has its reason in the varying inclination of the schistosity of the areas, but also stems from an increasing stability of the NE-area based on higher cohesion values and a more beneficial friction angle (Poisel et al., 2016). Additionally, the instable SW-section contains greater amounts of retrograde biotite, which acts as a lubricant and facilitates further slipping, whereas the NE is structurally influenced by the appearance of z-folds that rather function as consolidating components of the rock fabric. A NW-SE striking, lateral boundary plane acts as a vertical fracture plane separating the more stable from the less stable zone (Poisel et al., 2016).

The geodynamic situation of the former quarry Fehringer is well described by Poisel et al., (2016). Via structural measurements with the assistance of a drone and a software called Shape MetriX^{3D}, they concluded that the region is dominated by top-to-the-SE shearing and that the quarry can be subdivided into three homogenous areas (Fig. 4). In area 1 drag folds dominate, with their the axial surface gently dipping in WNW, making the folds approximately subvertical striking ESE. Area 2 contains the main slip plane along which the rockslides occurred over the years, either by inappropriate excavation or precipitation. Structurally, this is mainly due to biotite-rich amphibolite layers containing shearbands that increase the

inclination of the slope in this area together with these layers acting as soft portions that emphasize slip (Fig. 4, light blue). Examples for these layers have been found in the rocks now chaotically scattered around after a multitude of these rockslides in the past (Fig. 5 c). Slickensides dipping SE appear, most likely originating from the numerous occassions of mass movement. Area 3 does not show any of the abovementioned features like folds or shear bands but just contains the general SE dipping of the layer.

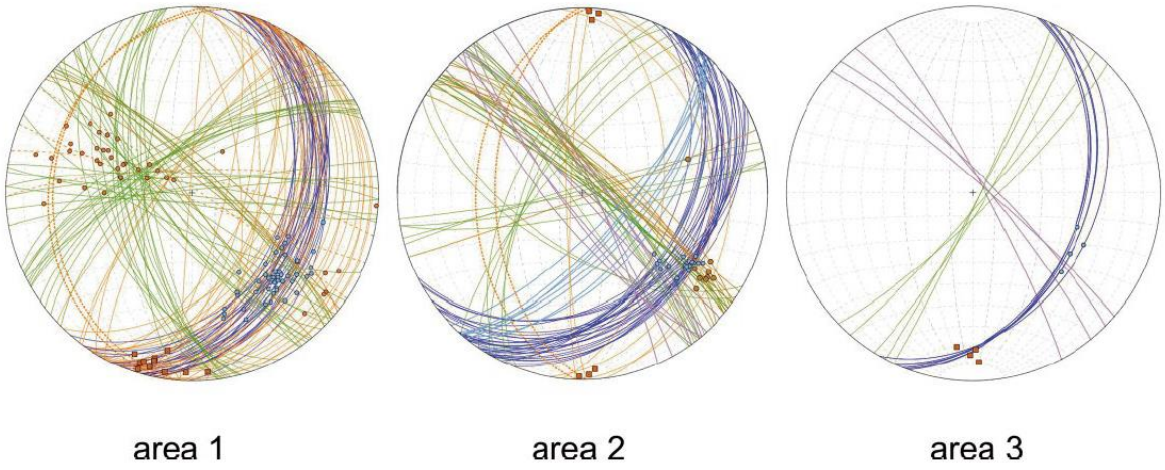

Fig. 4 Geological structures in the area according to Fig. 3; foliation (blue) and folded foliation (orange), shear bands (light blue), dykes (purple), joints (green), karst crevasses (brown); after Poisel et al., 2016, Fig. 3

Methods

Sample Preparation

Mutliple samples were collected at the quarry Fehringer to gather various boudin-types appearing at the site in order to characterize boudin structures, get a better idea of the flow regime and identify active deformation mechanisms. Due to abundancy of different boudin types (Fig. 5), two Boudin End-Members were established in the following named Type 1 and Type 2, both representing a different kind of deformation behaviour. Various samples representing one of the two End-Members were analysed by the same work flow.
Before cutting the rocks, photos were taken of each sample from different perspectives for documentation purposes. Then the samples were cut parallel to their lineation and perpendicular to the foliation allowing for a more detailed macroscopic description of the rocks (Fig. 5). Finally, the samples were cut to appropriate size in order to make thin sections of varying dimensions (4.35x2.75 cm, 5x5 cm, 15x10 cm) with a thickness of ~ 30µm. Thin sections chosen for further investigation via SEM and EBSD were chemomechanically polished with an alkaline colloidal silica suspension (Syton©) and carbon coated in order to establish electric conductivity.

Optical Microscopy and Thin-Section Scans

The thin-sections were used for analysis under the optical microscope (Leica DM4500 P). The samples were investigated based on their mineral composition and microstructures. Through a mounted camera, photos were taken under plain and crossed polarizers as well as reflected light for documentation. Additionally, the thin-sections were scanned with a Nikon colour-negative CoolscanV ED scanner to receive a proper overview of the individual thin-sections of the samples. These scans were later used as an orientation reference for the location of grain size, Phase and EBSD maps.

Grain Size Maps, Phase Maps and Element Distribution Map

Grain size and phase maps were generated on the basis of backscatter electron (BSE) images in order to identify potential variation in grain size and phase distribution with respect to the boudinaged aplite dyke. The FEI InspectS SEM (Department for Geodynamics and Sedimentology, University of Vienna, Austria) was operated at an acceleration voltage of 10 kV, a spot size of 5 at a working distance of about 10 mm and a magnification of 147x. Initially, the thin-section scans were used to locate every significant feature of the respective sample, the most important one being the boudinaged aplite and its transition into the marble host rock. These areas were then analysed by profile sections in the form of vertical rectangles. The resulting profiles consist of multiple rows of BSE images stitched together vertically, which again are each constituted by three individual images that are aligned horizontally. This

arrangement makes it possible to create BSE profiles that serve as basis for grain and phase-distribution analysis. In order to digitalize and visualize the grain boundaries, they were manually drawn on the basis of the original BSE image. The drawn grain boundaries then could be analysed via the Software *ImageJ*, capturing every closed grain in the section and automatically analysing grain area, aspect ratio and orientation of the longest axis (Heilbronner and Barrett, 2013). Based on grain-boundary maps, colour coded grain size Maps were generated using *ImageJ* for better visualization of grain size variation (Heilbronner and Barrett, 2013). For the generation of colour coded phase maps, the BSE profiles were imported into the Software *CorelDRAW X7*, which makes it able to discern between different grey values and group matching polygons according to their exact RGB-Value. The grey-values of these polygons are representative for a certain mineral and can be re-coloured, resulting in a phase map for the entire profile section. This method is vital in quickly noticing trends or tendencies regarding the mineralogical composition of the sample. An Element Distribution Map done by EDX was created for a chemical quantification of certain areas featuring interesting aspects of the samples. These maps were generated on the FEI InspectS SEM (Department for Geodynamics and Sedimentology, University of Vienna, Austria) with an acceleration voltage of 15 kV, a spot size of 5 at a working distance of about 10 mm and a magnification of 875x. The analysed section was evaluated based on the following elements: Al, Ca, K, Na, and Si to receive more information on transition zones, resolve possible reactions between different minerals and find out if there is any internal chemical zoning. A number of SEM-BSE detail images were created under the same conditions as used during the EDX-Mapping with higher magnification. The purpose of these images was to register conspicuous structures and phenomena to act as references or examples for certain processes.

Grain Analysis

Digitized grain size Maps were used to automatically generate statistical values in *ImageJ*. Two regions of two investigated samples, representing Type 1 and Type 2 respectively, were compared. The *Host Rock* region, with greater distance to the aplite, and the *Rim* region, right next to the aplite, to identify possible variation in grain size and grain orientation.

The 2D orientation of the grain long axes with respect to horizontal of the sample are plotted in rose diagrams using the software *TectonicsFP*. Data have been plotted using a clockwise interval of 10°. The data was then rotated by 90° since *ImageJ* calculates from a different point of origin compared to *Tectonics FP*.

Values for the grain area were obtained from *ImageJ* and further processed using *Excel.* The grain size was then calculated by means of the equivalent diameter:

$$\mathrm{d} = 2\sqrt{\mathrm{A}/\pi}$$

The distribution of grain size is plotted in histograms using a binning of 60 µm.

Electron Backscatter Diffraction (EBSD)-Mapping

Crystal distortion and crystallographic orientations were quantified by EBSD mapping performed on a SEM FEI Quanta 3D FEG equipped with a SE-, BSE-, EDX- and EBSD-detector (Department for Lithospheric Research, University Vienna, Austria). The SEM was operated at an accelerating voltage between 10-15 kV, a beam current of 100 nA in analytical modus using a spot size of 1, a working distance of 14 mm and a sample tilt of 70°.

Three comparable regions on representative samples for Type 1 and Type 2 boudins have been mapped using a step size ranging from 1.7 to 3.5 µm. The zones of interest were the *Host Rock*, the *Rim* area close to the aplitic dyke and the aplite itself referred to as the *Core*. For the first two of these regions of both Type 1 and Type 2 the calcite was analysed, while in the *Core*, quartz and albite have been analysed, representing the dominant phases in the aplitic dyke.

The OIM Data Analysis software has been used for data processing. The EBSD data have been cleaned by means of neighbour 0-2 and confidence index (CI < 0.1) before used for further analysis. Grain boundaries were defined with a misorientation angle larger than 10° between adjacent points and a stepsize of 5 Pixel. Everything below 10° misorientation will be referred to as low-angle grain boundary. Intracrystalline distortion in terms of misorientation has been analysed and visualised using two different mapping types.

The first map type assigns a misorientation value to each grain corresponding to its average misorientation (Grain Average Misorientation). This approach gives a good impression of the general magnitude of misorientation, however, it can overshadow localised crystal distortion. The second map type (Misorientation Deviation Angle map) colour codes local misorientations with respect to the grain average misorientation, allowing for the identification of zones of high (internal) misorientation.

Additionally, stereographic projections of c (0001) and +a (-1-120) axes and poles to e (01-18) planes for calcite; and c (0001), +a (-1-120) axes and poles to m (10-10) planes for quartz have been plotted. Data are plotted in contoured equal angle upper hemisphere projections.

Results

Structure Analysis - Macroscopic

The former quarry Fehringer is mainly composed of a coarse grained calcite, silica-rich marble host rock. The marble got syntectonically intruded by aplitic and pegmatitic dykes, cross-cutting the marble foliation at various angles. Aplitic dykes are characterized by a homogenous milky colour and fine grain size while pegmatites show coarse grained feldspar and quartz. Dykes vary in thickness between 0.5 cm and 70 cm sometimes occurring in parallel to sup-parallel sets. These dykes often feature a dark halo at their rims. Sometimes black intercalated biotite layers form ESE-vergent Z-folds.

Regarding boudinage, the outcrop features various types ranging from Domino-Boudins (blocky types) to pinch-and-swell Structures (Fig. 5). Blocky or domino-type boudins (Fig. 5, a, b) exhibiting dark, central cracks acting as the inter-boudin zone after the aplitic layer was torn apart (Fig. 5 a). Additional cracks can occure, although these are often not fully penetrating the aplite (Fig. 5 a). Once detached from the neighbouring boudin segment, single segments can exhibit a higher degree of rotation (Fig. 5 f).

Next to the massively looking blocky boudins also thinned out aplite portions can appear, exhibiting a different deformation behaviour (Fig. 5 b). Tapering boudins are an example for a boudin End-Member deforming continuously (Fig. 5 c). Dark, frayed portions encompassing the aplites represent former layers of biotite torn apart. In between the boudinaged lenses, precipitations of quartz can be observed. Another boudin type exhibiting continuous deformation are pinch-and-swell structures, featuring gradually thinned out aplitic layers that can become folded in their thin, centre portions (Fig. 5 d). Greyish and reddish regions appearing in the marble are either enriched or depleted in Fe^{3+}. The red iron seam around the aplite acts as a passive marker and traces the flow pattern of the host rock in the vicinity of the aplite. Cracks or inter-boudin zones are often centres for mm-cm wide translucent quartz lenses (Fig. 4 d). Necked boudins are characterized by their rectangular shape and feature quartz fillings in their respective inter-boudin zones (Fig. 5 e). Around these inter-boudin zones the marble host rock shows flowing patterns directed towards the centre of these areas. Thinner aplitic layers close to these regions can become folded with their axial planes parallel to the length axis of the inter-boudin zone (half folds or *scar folds*, Hobbs et al., 1976). Below the main necked boudin train this sample also contains an additional aplite dyke, again signifying the importance of aspect ratio during the process of deformation and how the dykes are acting upon it (Fig. 5 e). Locally highly chaotic boudin trails can be observed (Fig. 5 f). Blocky segments are strongly rotated once detached from their neighbouring boudin segment making it difficult to detect the original dyke location. Such boudin trails sometimes exhibit late folding (Fig. 5 f).

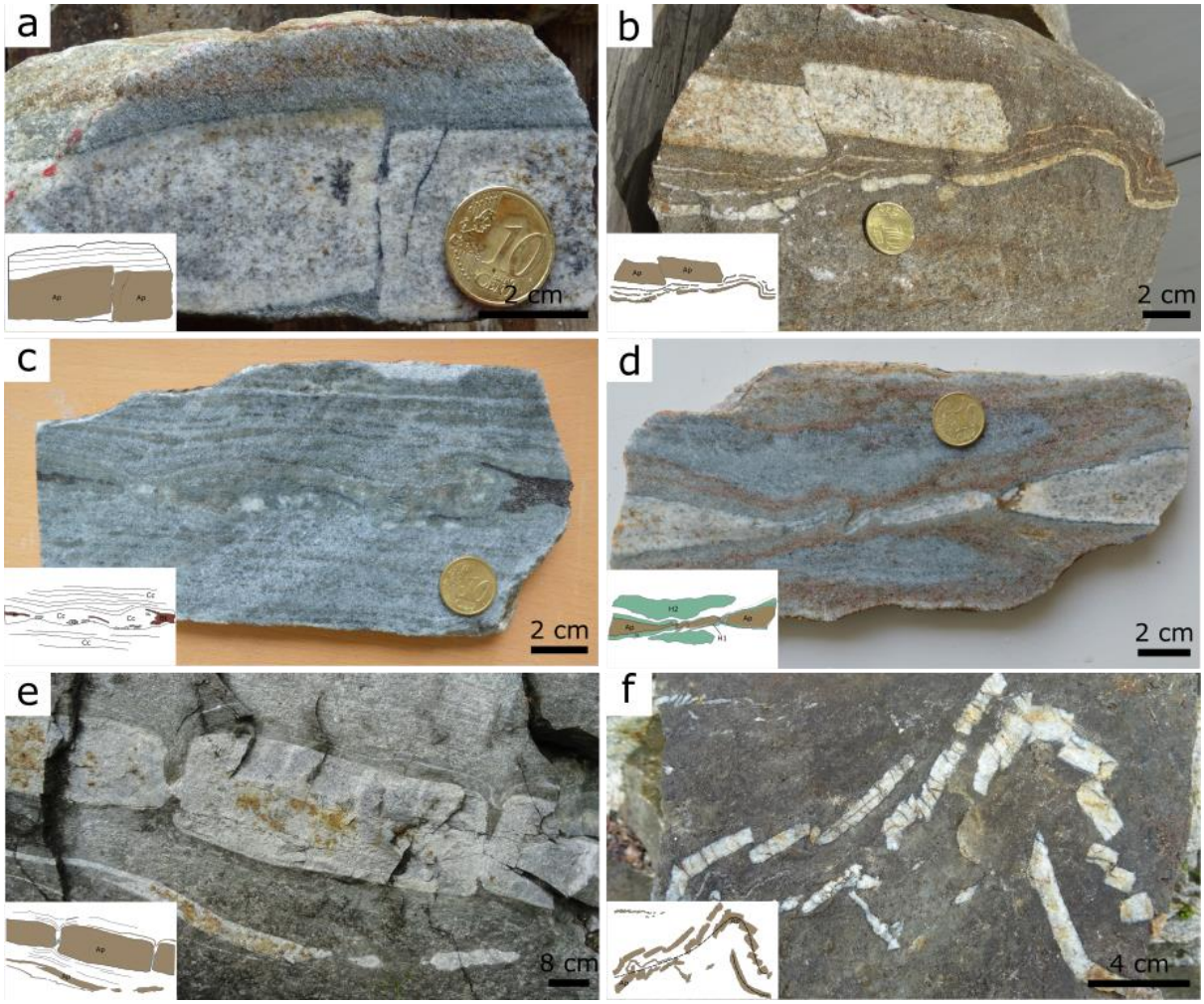

Fig. 5 Sample and outcrop images marking the variety of boudin-types that are met at the investigated site.
a) Segments of domino-boudins exhibiting a monoclinic symmetry resulting from rotation after decoupling.
b) Example for a domino-boudin in a 4 cm thick aplitic layer. Note the folding of the thinner layer below the boudins.
c) A splayed boudin with frayed ends of a former biotite layer transversing the host rock; the inter-boudin zones show accumulations of quartz.
d) Shortened pinch-and-swell structure where the thinned *pinch* is folded together. A reddish oxidation seam acts as passive marker, tracing the host rock deformation in the vicinity of the aplite.
e) A necked boudin with feldspar filled inter-boudin zones. Suction forces in these inter-boudin zones deformed the marble host rock and thin aplitic layers into tight neck-folds.
f) Folded boudin train where the chaotic boudinage structures probably resulted from rotation and clustering of segments of a boudin train of finite length.

Structure Analysis - Microscopic

Confronted with this abundancy of boudin-types it was decided to focus on two end members for the microstructure analysis in order to identify common or differing phenomena and structures, helping to identify active deformation mechanisms during boudinization. Both sample sets are investigated in the same manner by the same methods to create reproducible results that would allow for a better understanding as to why there is such a great number of boudinage forms in such a limited amount of space.
The two End-Members, which are compared with each other are samples of the blocky- or domino boudin type in the following referred to as Type 1 (Fig. 5 a, b) and a pinch-and-swell structure referred to as Type 2 (Fig. 5 d).

Microfabrics Type 1-Blocky-Domino Boudin

The blocky boudin type is represented by two different samples showing quite similar deformation behaviour (Fig. 6).

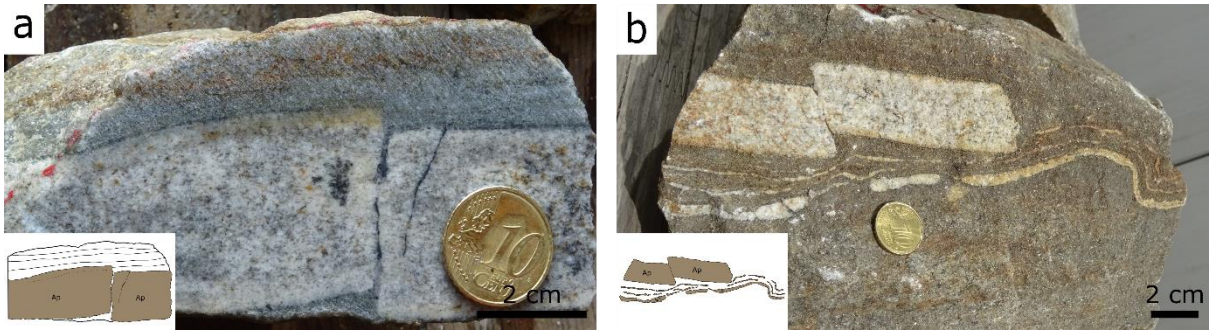

Fig. 6 Two hand specimens constituting the Type 1-Blocky-Domino Boudin
a) Domino-block boudin with a central crack filled with precipitated minerals e.g. quartz and chlorite
b) Another domino-block boudin with thinner aplite dykes below being folded and stretched

The calcite grains constituting the marble host rock have a grainsize ranging from >100 µm to 1 mm. Microscopical analysis has shown that there is a higher abundancy of smaller grains in the vicinity of lithological transition between the marble and the aplite. This can be seen under the microscope as well as on scans of the thin sections (Fig. 7 and 8). Another frequently appearing characteristic is a dark diopside rim (Fig. 5) surrounding the aplitic and rarely pegmatitic dykes. Macroscopically this diopside can be observed as a black seam encompassing the boudin segments with a thickness of 50-300 µm (Fig. 6 a, b)

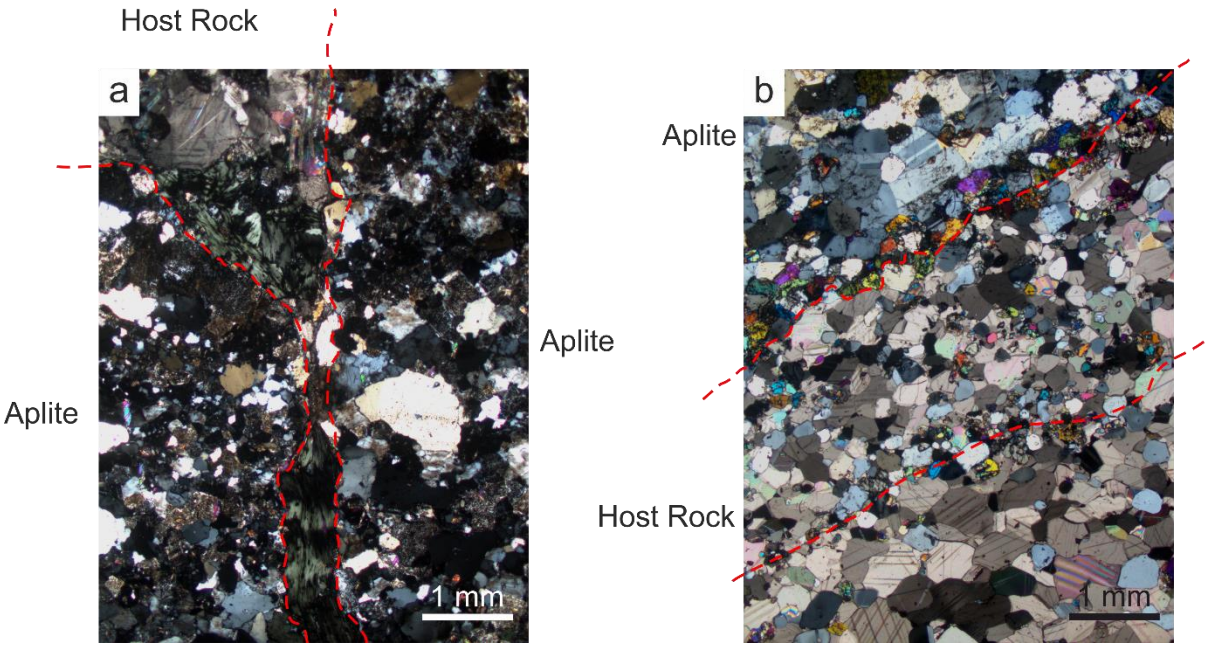

Fig. 7 Two microscopical images under xpl showing chlorite (a) and a zone of lithological transition (b)
a) Central crack of sample a in Fig. 6 crack showing two chlorite crystals, the left one being strongly deformed, the right one displaying distinct kink bands.
b) A c. 3 mm transition zone of the marble along the margin of the aplite (top) records reduction in grainsize of calcite. Note the diopside seam (dashed line).

The halo occurs on every side of the boudin segments except along inter-boudin zones. Diopside is generally scattered throughout the whole host rock in a seemingly random fashion and usually appears in concentrated clusters, although single grains are also present. Internal cracks inside the boudin segments represent zones for minerals to precipitate in, e.g. chlorite or quartz. The chlorite appears as either heavily deformed or with distinct kink bands but can remain relatively undisturbed as well (Fig. 7 a).

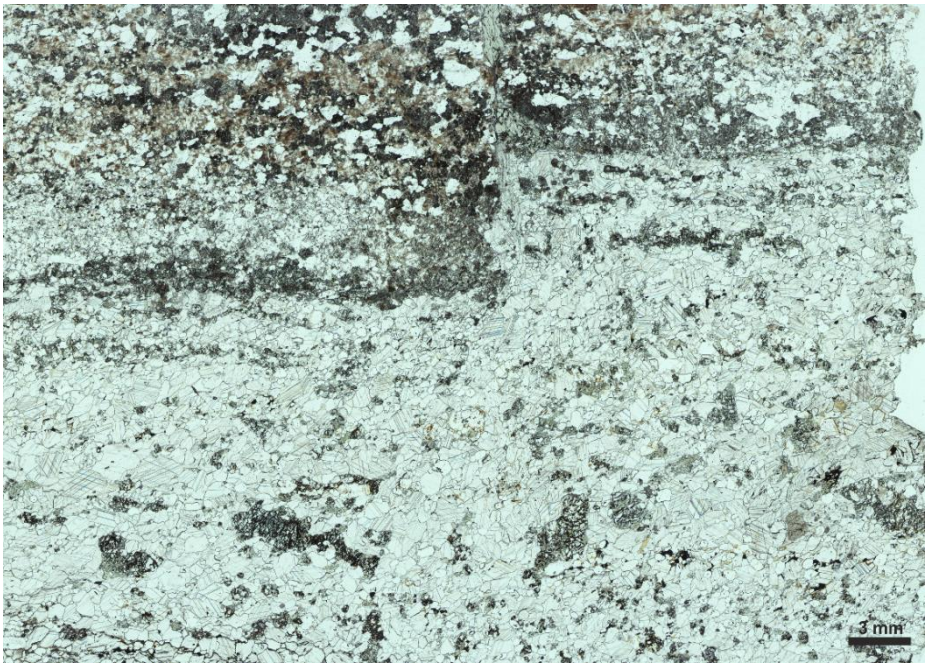

Fig. 8 A thin-section scan of the Type 1 sample in Fig. 6 a right showing the central crack as well as the transition zone from the host rock (bottom to mid) to the aplite (top)

Some calcite grains show signs of undulose extinction, but it does not represent a significant feature in the rocks. The grain size Map of the analysed section representing Type 1 doesn't reveal any tendencies of how grainsize is varied in the course of the sample (Fig. 10). Therefore, it doesn't seem to confirm the observation of a decrease in grainsize close to the aplitic dyke, judging by the diameter of the grains at the bottom section of the profile with maximum distance to the aplite (at the chosen boundary conditions). However, it does show the remarkable size of the orthoclase grains, inside the two cross-cutting aplite dykes in comparison to the relatively finer grained calcite grains that make up the host rock (Fig. 10).
The phase maps, as well as the grain size Maps further emphasize the comparatively larger grainsize of the orthoclase as well as an SPO of the calcite grains going approximately ENE-WSW (Fig. 10). The previously mentioned diopside grains distributed throughout the marble, not only align along the main dykes transecting the marble but likewise concentrate along scattered boudin segments of former dykes. Furthermore, the aplite follows a similar behaviour as diopside regarding its appearance in the host rock. It exhibits a very high concentration especially at the lower parts of the phase map and also is present along the rims of the dykes. The shape of the quartz grains in the centre of the aplite is usually patchy or bulky and appear transparent in the thin section, contrasting the orthoclase covered by a noticeable, characteristic brown *mush* corresponding to suassuritization.

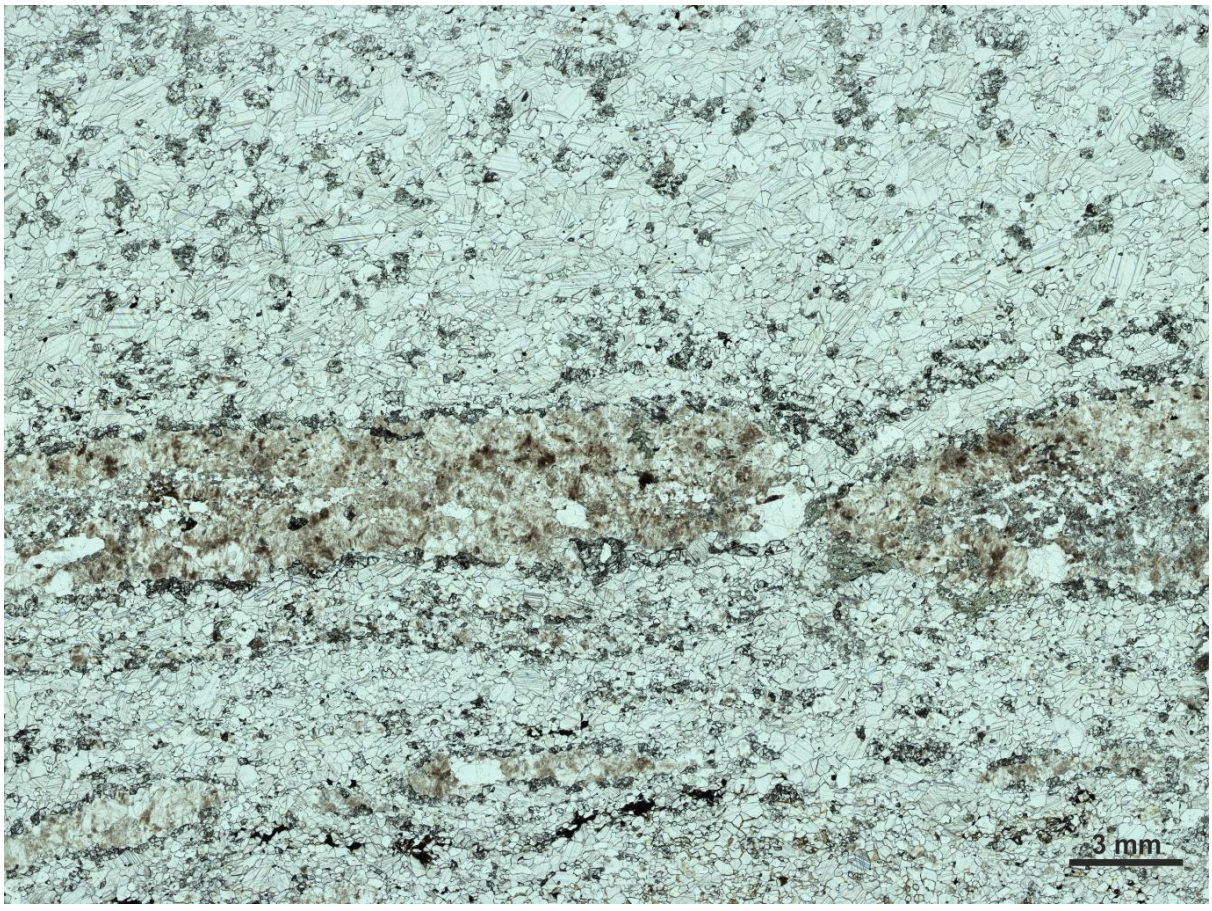

Fig. 9 Scan of a thin section of the left sample seen in Fig. 6 with a rectangle marking the section analysed by the SEM

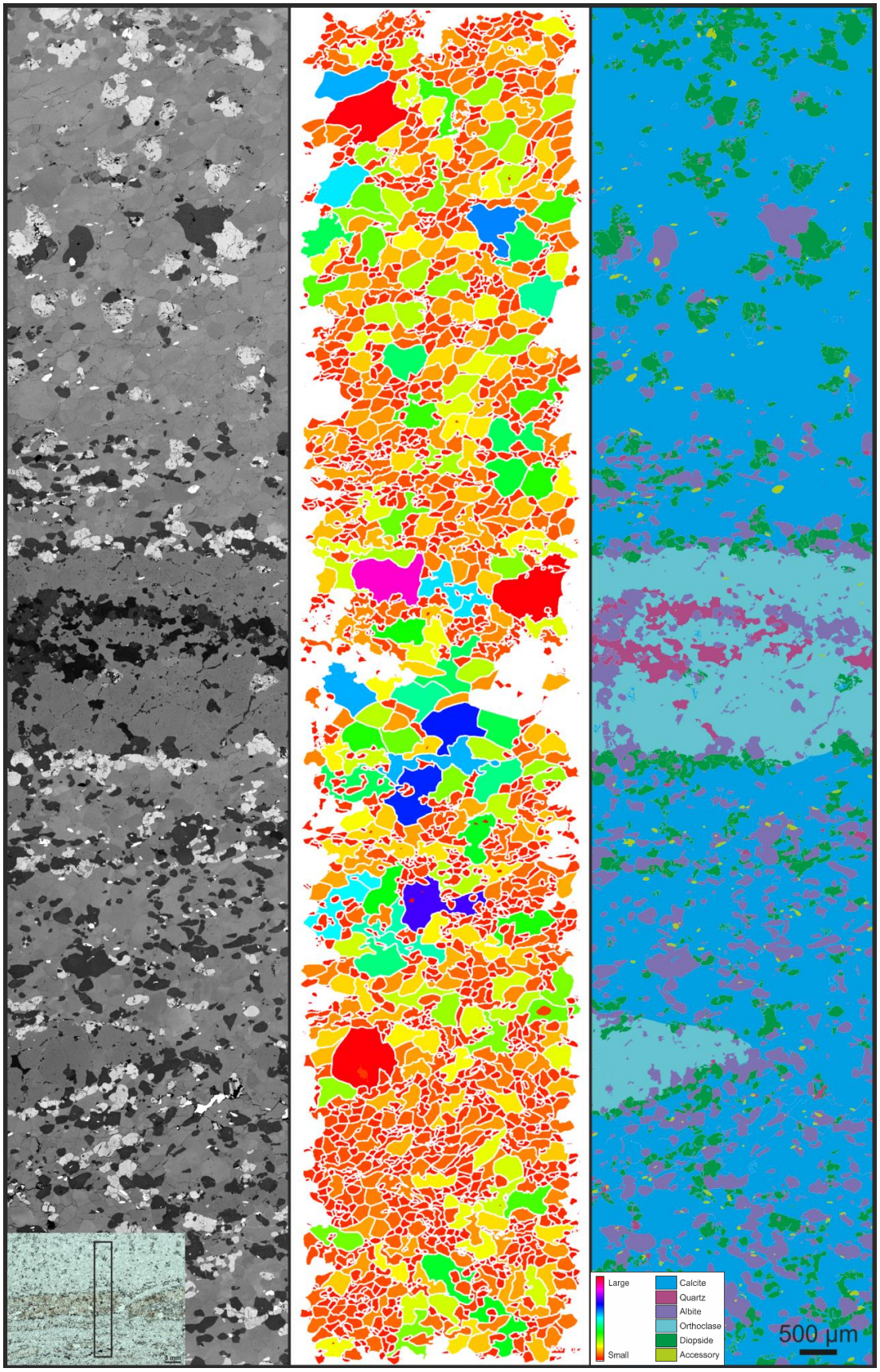

Fig. 10 A complementary image consisting of three columns representing different properties of a vertical SEM-Profile done for Type 1: Left: The original SEM-BSE image with different greyscale-values; Middle: Colour-coded grain size Map; Right: A phase map which attributes a colour to each mineral phase. Bottom Left: A scan of the used thin section with the investigated area marked by a black rectangle. Bottom right: Legend for the grain size Map and the phase map respectively

SEM-Detail images reveal the distribution of albite along grain boundaries but also appearing as lamellae throughout the orthoclase (Fig. 11 a). The quartz and the albite appearing in the aplite are often not easy to differentiate from each other under the SEM due to their behaviour, which makes them appear to be mingling of some sort, although this is only a visual and not chemical impression (Fig. 11 a). Some feldspar grains exhibit a chemical zonation, whereby the core contains Ca and Na representing plagioclase and the rim contains no Ca and therefore appears darker under the SEM (Fig. 11 b). A rare microstructure occurring in the aplite are myrmekites. The term was first coined by Sederholm (1899) and represents an intergrowth of quartz and feldspar, in this case albite (Fig. 11 b; Abart et al., 2014). These structures mark an exception through the rock history and were only discovered once during the SEM-Analysis.

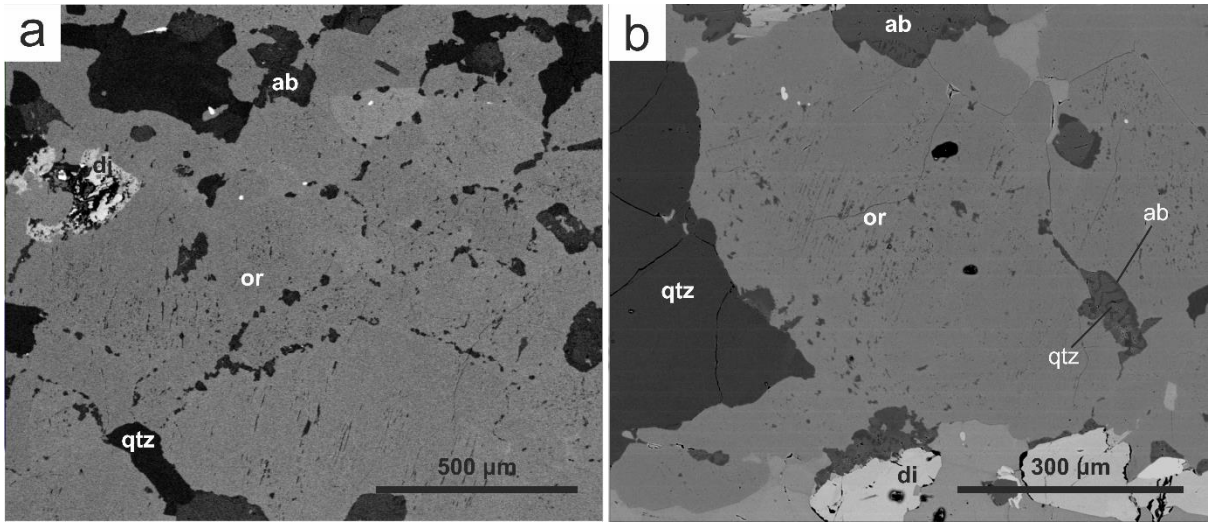

Fig. 11 BSE-Detail-SEM images featuring the varying appearance of albite
(a) and displaying zoned plagioclase grains together with myrmekite
(b) Abbreviations stand for the following: albite (ab), orthoclase (or), diopside (di), quartz (qtz)

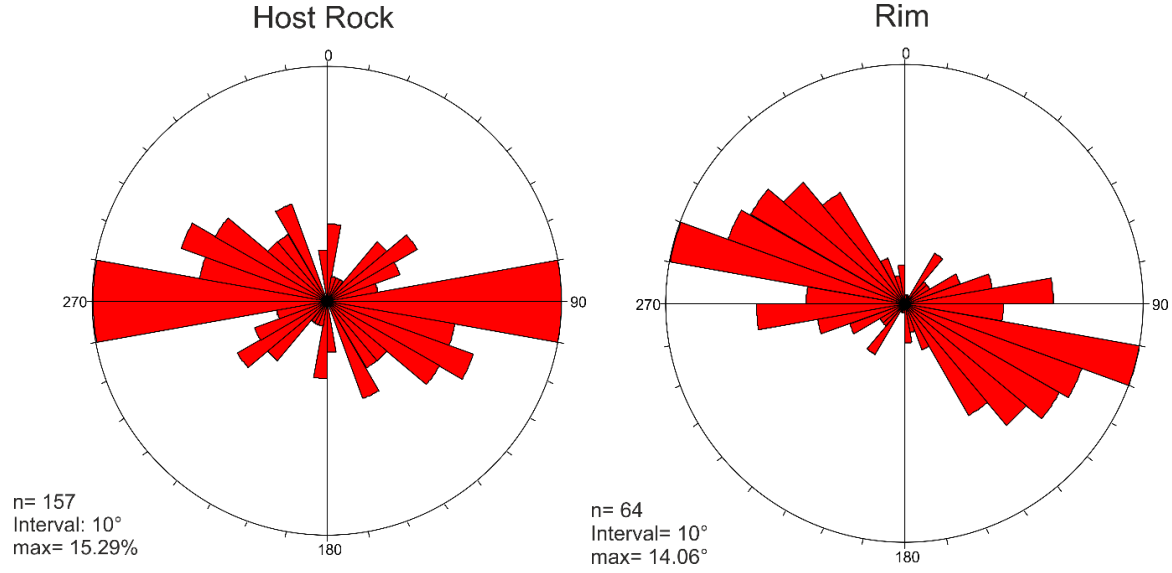

Fig. 12 Rose diagrams showing the 2D orientation of long axes of calcite grains in the *Host Rock*/*Rim* areas of sample b in Fig. 6.

The Rose diagrams evaluating the SPO of the calcite show a disparity of orientations depending on the analysed section (Fig. 12). There is slight deviation in the orientation of the grains but a general trend can be established. While the *Host Rock* is mainly oriented E-W the *Rim* region shows an ESE-WNW orientation.

When it comes to the grainsize analysis depicted in the form of two histograms there is a higher number of smaller grains in the vicinity of the aplite (*Rim*) and more, larger grains in the more distanced *Host Rock*, but the distribution is not unambiguous (Fig. 13). Of a total of 157 measured grains in the *Host Rock* more than 80% lie within the range between 60 and 240 µm. The remaining 20% make up the middle to larger grainsizes of >240 µm. Very large grains, with i.e. >600 µm, make the exception and are relatively rare. Therefore the distribution shows a steady decline in the abundance of grains with increasing diameter of the measured calcite. The greatest amount of grains in a single binning step is at 120 µm containing 37 grains, closely followed by 60 µm with 36 grains, meaning almost 50% of the measured grains lie within this area.
At the *Rim* Section a total of 57 grains were measured, also showing a high abundancy of comparatively smaller grains. Over 90% of these grains lie within range of 240 µm. The largest grain obtained for the *Rim* has a diameter of 380 µm. Even though the number of grains measured for the *Rim* is considerably smaller, the distribution looks similar to that of the *Host Rock*

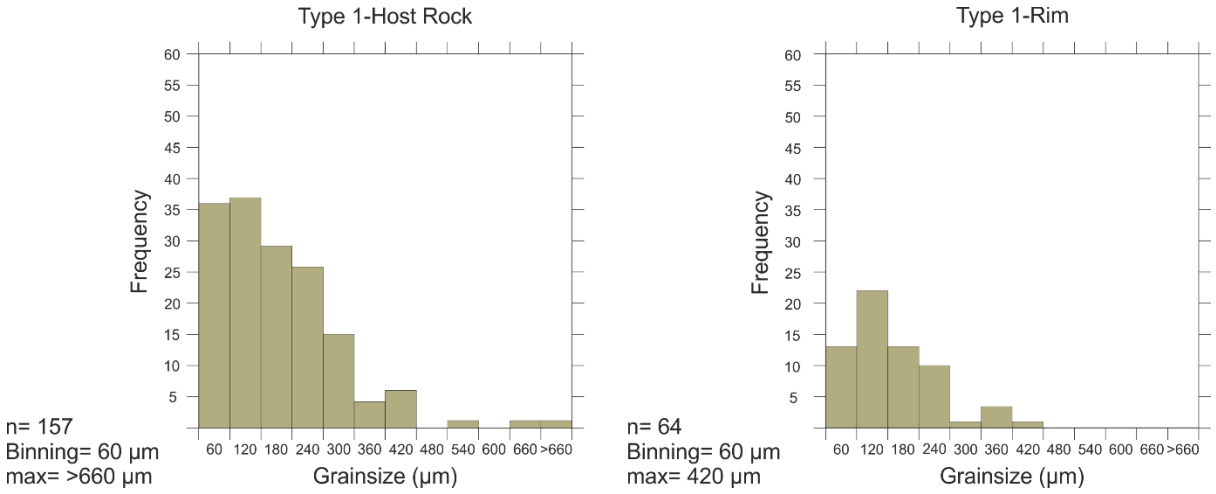

Fig. 13 Grainsize Histogram of the *Host Rock* section (left) and the *Rim* (right) section of sample b in Fig. 6.

The EBSD analysis of the three regions, *Host Rock*, *Rim* and *Core* shows varying misorientation based on the measured location. These sections were located with the assistance of a thin-section scan of the investigated sample and labelled by three coloured rectangles (Fig. 14). The first zone being analysed is the *Host Rock* region, showing an average misorientation between 0 and 5 degrees, which is the range used for every investigated section regarding their average misorientation. A couple of grains are almost free of any misorientation indicated by their light blue colourization and the highest degree of average misorientation found in the section amounts to 3.1° (Fig. 15 a). Furthermore there is only a small number of subgrain boundaries, compared to the *Rim* zone, which not only features a high number of the latter but also a greater abundancy of deformation twinning. The average misorientation of the *Rim* (Fig. 15 c) has a maximum of 4.9° and is generally more pronounced throughout the area compared to the *Host Rock*. Looking at the misorientation deviation, the *Host Rock* exhibits only few centres of heterogeneity where the misorientation is increasing to values of 10-15° but has one maxima of 31° (Fig. 15 b). The *Rim* section displays more zones of localised enhanced misorientation, reaching an utmost value of 29° (Fig. 15 d). Similarly to the average misorientation the misorientation deviation is higher and more intensively distributed in the *Rim* compared to the *Host Rock*,

The *Core* region, featuring quartz instead of calcite since this is past the transition zone and already inside the aplite, exhibits only low amounts of average and localised misorientation similarly to the *Host Rock*. However, certain grains in the *Host Rock* display an average misorientation of about 3°, whereas the average misorientation in the *Core* has utmost values of 1.1°, indicated by the dark blue colourization of the grains (Fig. 15 e). Therefore, the average misorientation is lowest when compared to the other regions and even though the quartz is not homogenous in its misorientation deviation there are only few zones that differ from the general result (Fig. 15 f). These few zones have an approximate misorientation deviation of 4-5°, although it can climb to 7.2°.

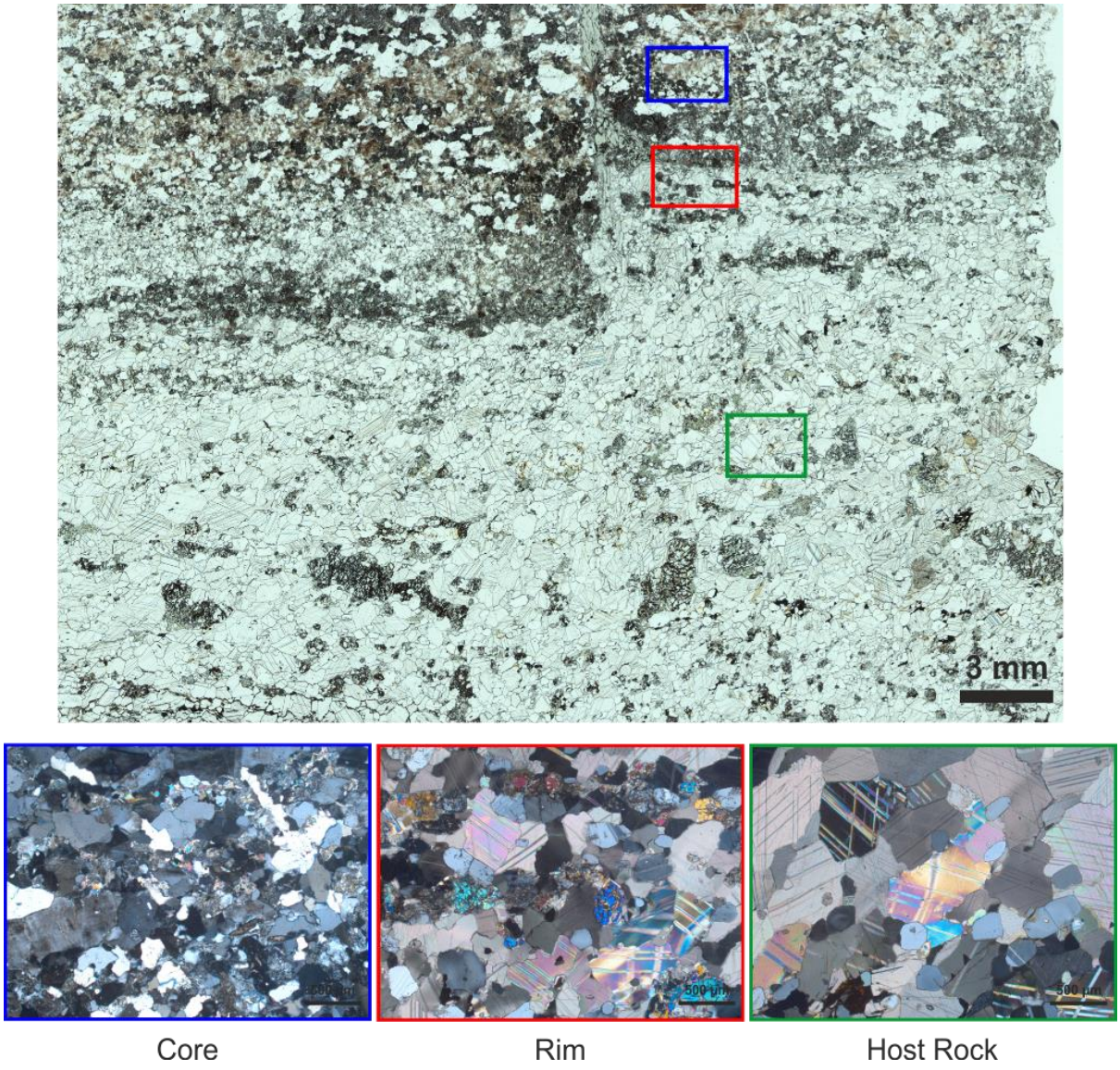

Fig. 14 Thin Section scan of sample a in Fig. 2 with three marked regions (coloured) symbolizing the sections analysed by EBSD

The Pole figures of calcite in the *Host Rock* (Fig. 16) display a relatively uniform alignment of the +a-axis parallel to the foliation assuming a girdle-like shape, whereas the c and e-axis show a preferred alignment normal to the foliation. In the *Rim* neither of the plotted axes follow a certain pattern besides of the c-axis where a slight orientation parallel to the SPO can be observed. The *Core* region maintains a chaotic distribution throughout making it impossible to deduct specific trends or patterns in any of the plotted axes (Bestmann et al., 2006; Wilson et al., 2007).

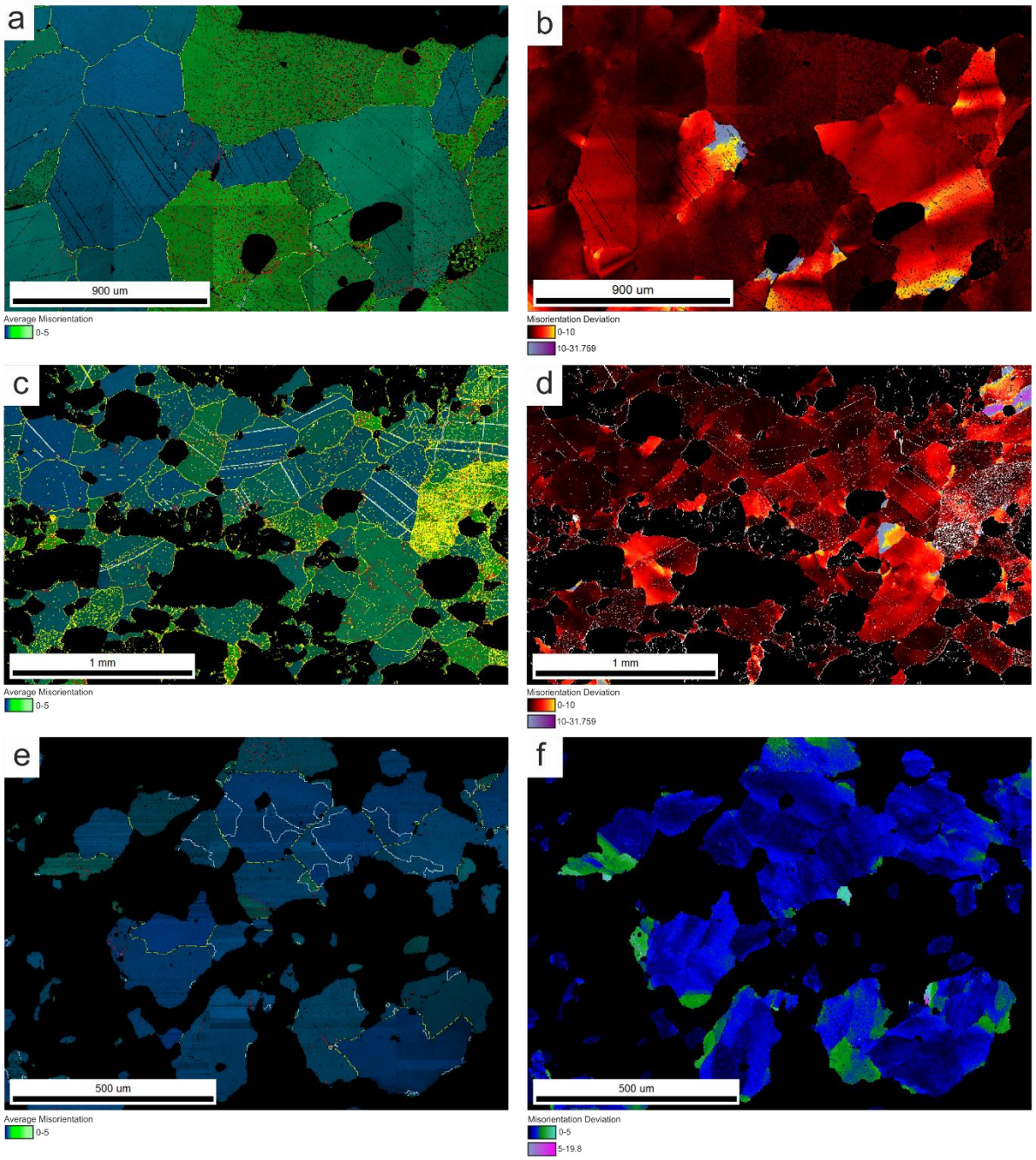

Fig. 15 Grain average misorientation and grain boundary map (left) and misorientation deviation angle map (right); Top to bottom: *Host Rock* (Cc), *Rim* (Cc), *Core* (Qtz); Grain Boundaries: 2-5° (red), 5-10° (violet), >10° (yellow), Twins (white); see text for detailed descriptions of a-f

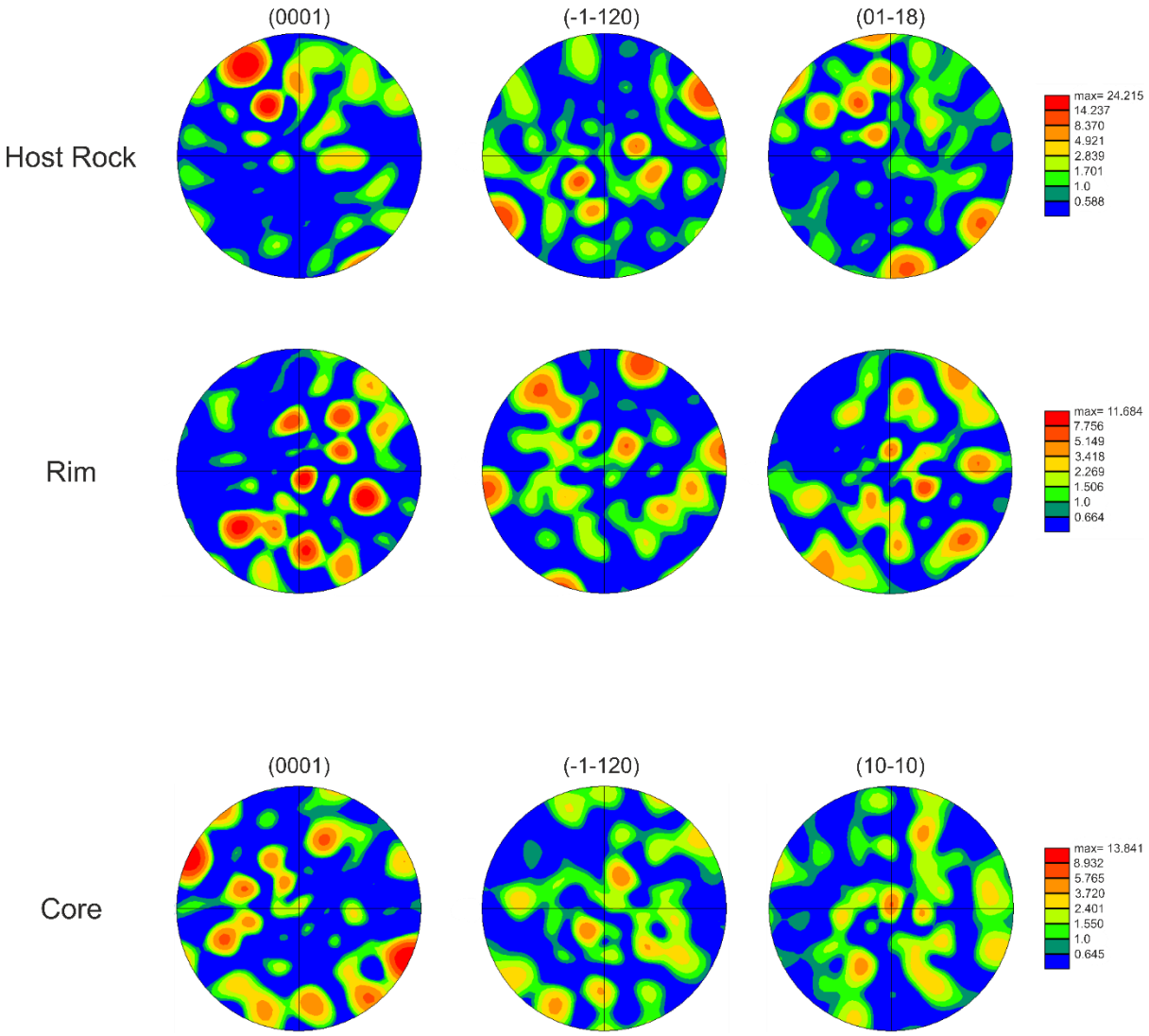

Fig. 16 Pole figures for the sections *Host Rock* (top), *Rim* (mid), *Core* (bottom) of Type 1 with their respective legends on the right; Analysed planes from left to right: Calcite: c, a, e; Quartz: c, a, m

To sum up some of the major points regarding the Type 1-Blocky-Domino Boudin:

- Cracks and/or inter-boudin zones give room for minerals to precipitate (e.g. Chlorite with kink bands)
- Possible grainsize reduction with increasing proximity to the aplitic dyke
- Change of SPO correlating to the location in the thin section of the sample
- Calcite average misorientation is higher at the *Rim* (4.9°) compared to the *Host Rock* area (3.1°)
- Calcite grains in the vicinity of the aplite show the highest misorientation deviation (29°), with the exception of a couple µm wide zone in the *Host Rock* (31°)
- Quartz grains in the *Core* show local internal changes of misorientation, although it‘s minimal
- Neither quartz nor calcite show a CPO
- The deformation seems to be concentrated at the transition zone between aplite and host rock

Microfabrics Type 2-Pinch-and-Swell/Tapered Boudin

Type 2 is represented by the following two samples (Fig. 17).

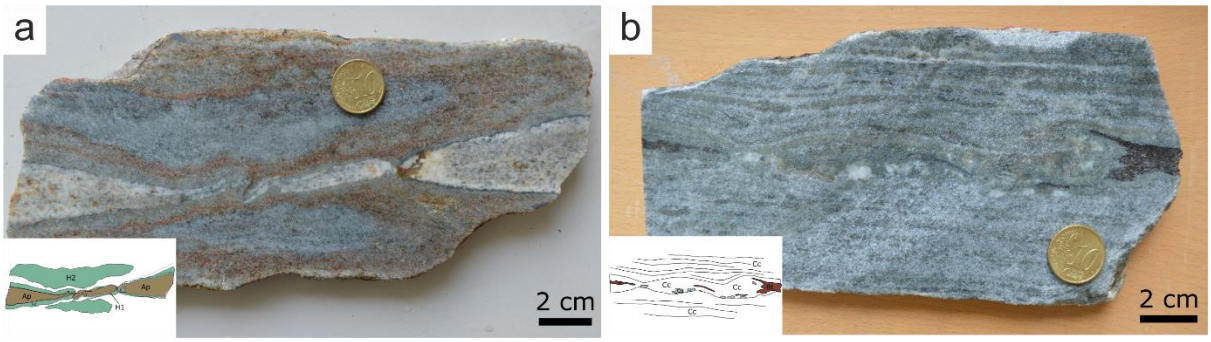

Fig. 17 Two hand specimens representing the Type 2-Pinch-and-Swell/Tapered Boudin
a) Pinch-and-swell structure with folded centre part
b) Tapered boudin with biotite fringes on either side

The marble host rock is characterized by coarse grained calcite and randomly dispersed grains of diopside and albite. Microscopical analysis of the Type 2 the pinch-and-swell structure feature two main zones that can be distinguished. The key criteria in which these two areas are differing is their quartz content (Fig. 18, yellow arrows). In one portion of the structure named the *pinch*, quartz is virtually absent. The *swell* portion however, contains many quartz grains with a much smaller grainsize of <0.5 mm compared to the orthoclase crystals (1-2 mm) inside the aplite that tend to be much bigger than the quartz or aplite grains, especially at zones of lithological transitions. Diopside, marked by its high interference colour under crossed polarizers, appears in great amounts throughout the marble and aligns itself along the rims of the aplite similar to what can be observed in Type 1. There is also saussuritization appearing in the aplite, something that is generally very common throughout all samples. However, this saussuritization only corresponds to the dykes and never occurs in the marble host rock.

Scans of larger thin sections (15x10cm) reveal a wider area of the pinch-and-swell structure (Fig. 19). It signifies the continuous tearing of the aplite layer as seen earlier (Fig. 17 a). The green seams of diopside are very pronounced as well as the brownish Fe^{3+} areas.

The centre portion of the sample is marked by an almost detached slab, still in contact with the former dyke. It looks to have been rotated and is now connected to the aplite through a folding structure.

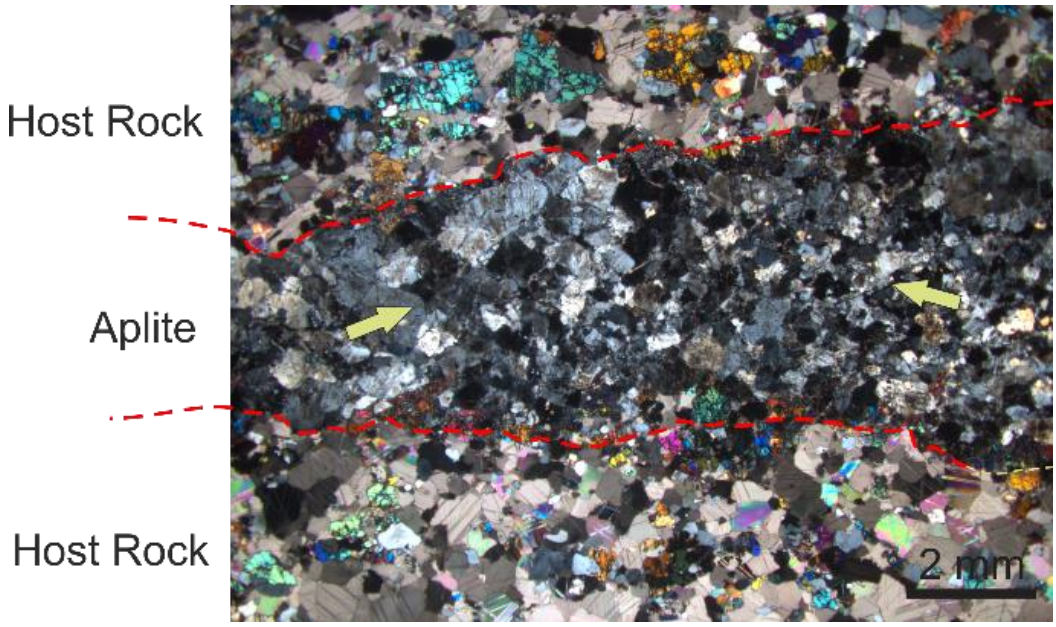

Fig. 18 *Pinch* (left half) and *swell* (right half) of an aplite dyke. The right *swelled* part consists of a core of mainly fine grained quartz and albite (right arrow). In the *pinched* left part this fine-grained core is absent and is composed of coarse orthoclase (left arrow). Additionally, dislocation glide and creep seem to be active

Fig. 19 A thin section scan of the pinch-and-swell sample seen in Fig. 17 a

For Type 2, two regions on the same thin section are being investigated to create a comparison of two areas of the pinch-and-swell structure (two rectangles in Fig 20).
The left rectangle shows the thicker *swell* zone, whereas the right rectangle represents the *pinch* portion. Dark grains or clusters represent diopside scattered throughout the host rock (Fig. 20). The diopside is concentrated on the transitions of the marble into the aplite and forms a ca. 0.5 mm thick boundary. The brown *mush* is only seen on the feldspar grains, whereas the orthoclase is mainly present at the outer parts of the aplite and the albite occurs in micro-cracks or as smaller grains throughout the whole pinch-and-swell structure. Quartz is mainly present as flat ribbons sub-parallel or slightly oblique with respect to the diopside seams (Fig. 20).

Fig. *20 Scan of a thin section of the sample seen in Fig. 17 a with a rectangle marking the section analysed by the SEM*

The grainsize map of the *pinch* section displays the large orthoclase crystals being especially pronounced at the rim areas of lithological transition. The grains of the calcite matrix appear to have a higher diameter on average compared to the host rock of the *swell* portion (Fig. 21). On a closer inspection of the phase maps, the centre of the *swell* portion is characterized by a fine grained mix of quartz (dark pink) and albite (purple). However, in the *pinch* region quartz is virtually non-existent. These two portions of the sample only lie part by about 1.5 cm, indicating a strong variance of mineralogical composition based on the location of the analysed area of the pinch-and-swell structure (Compare Fig. 21 and 22). In addition to the common diopside rims (green) along the margins of the aplite, there are further seams arranged above and below the aplitic dyke in close succession (Fig. 21). The albite appears in

the aplitic dyke as well as in the host rock. However, the portions in the calcite are also aligned along the rims and the additional seams that are striking parallel to the zones of lithological transition. Conjugated micro-cracks containing albite occur in the *pinch* part of the structure and show two types of orientations perpendicular to each other.

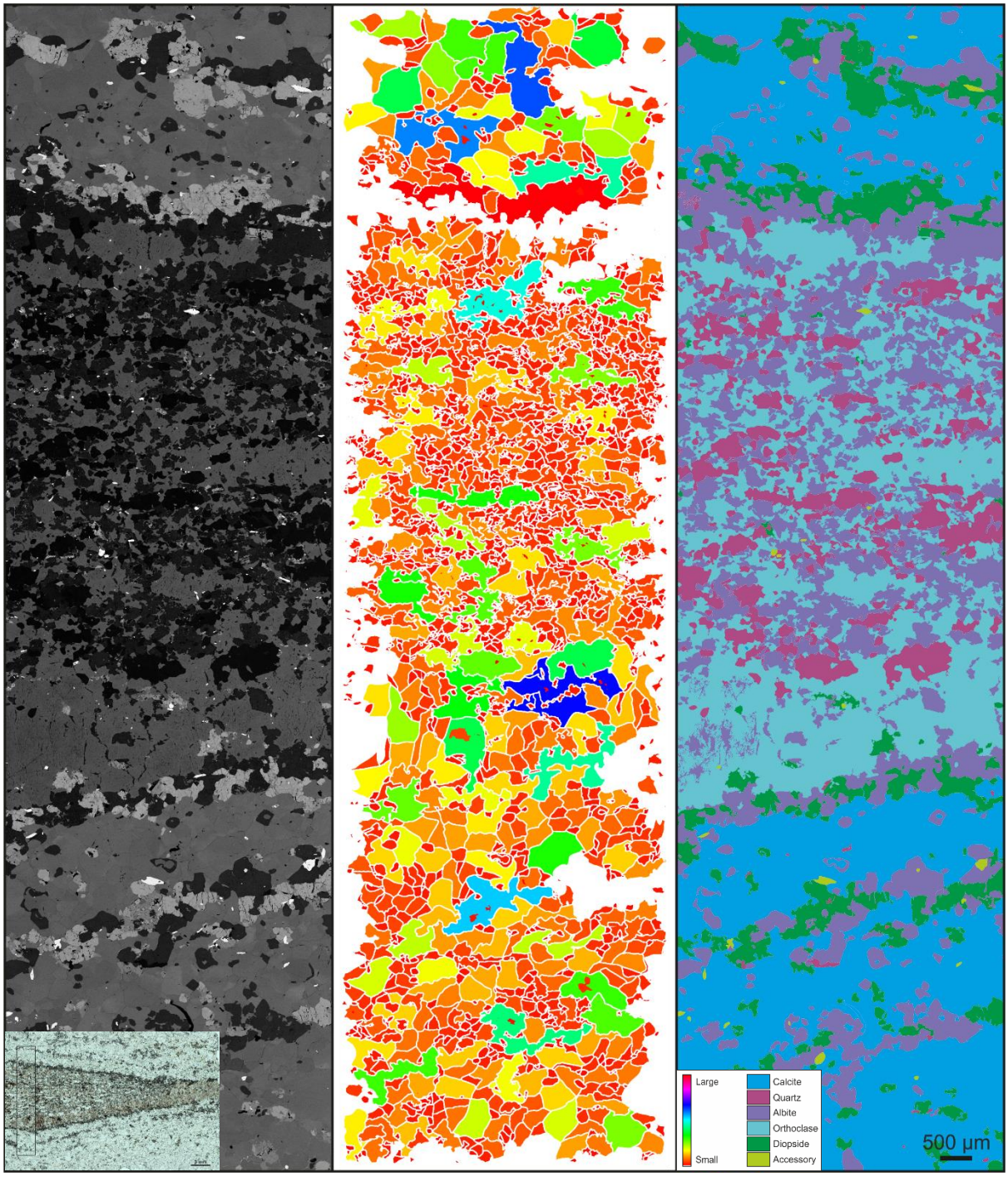

Fig. 21 A complementary image consisting of three columns representing different properties of a vertical SEM-Profile done for the Type 2 *swell* region: Left: The original SEM-BSE image with different greyscale-values; Middle: Colour-coded grain size Map; Right: A phase map which attributes a colour to each mineral phase. Bottom Left: A scan of the used thin section with the investigated area marked by a black rectangle. Bottom right: Legend for the grain size Map and the phase map respectively

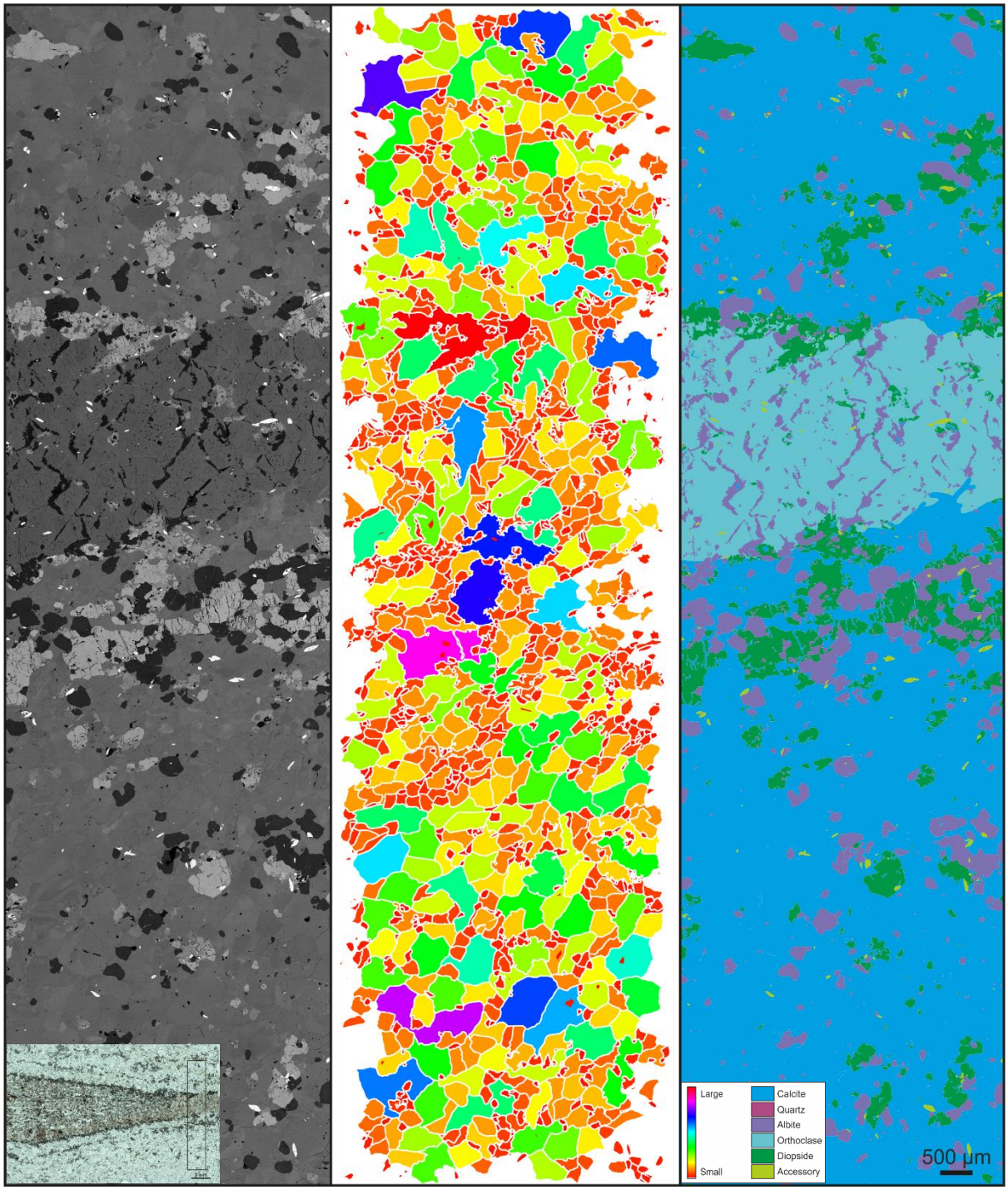

Fig. 22 A complementary image consisting of three columns representing different properties of a vertical SEM-Profile done for the Type 2 *pinch* region: Left: The original SEM-BSE image with different greyscale-values; Middle: Colour-coded grain size Map; Right: A phase map which attributes a colour to each mineral phase. Bottom Left: A scan of the used thin section with the investigated area marked by a black rectangle. Bottom right: Legend for the grain size Map and the phase map respectively

These conjugated micro-cracks in the *pinch* region of Type 2 have also been documented via Detail-SEM Images showing their orientation patterns more clearly and emphasizing the various ways albite is appearing in the rock. The mineral can occur as solitary grains in the marble host rock matrix (Fig. 23 a), as a couple µm thin lamellae in the orthoclase (Fig. 23 b) and finally in the form of the previously mentioned micro-cracks (Fig. 23 b). These micro-cracks and the *pinch* as a whole are both virtually devoid of quartz but very rarely small grains (~50 µm) can be observed. The EDX-Analysis of one of these cracks yields a quantitative chemical composition, Al being present in the entire section excluding the diopside. Ca is limited to the diopside whereas K only appears in the orthoclase. The results of the K-Map together with Na-Map greatly facilitate distinguishing the albite portion in the analysed section, showing the micro-crack itself encompassed by albite lamellae (Fig. 24).

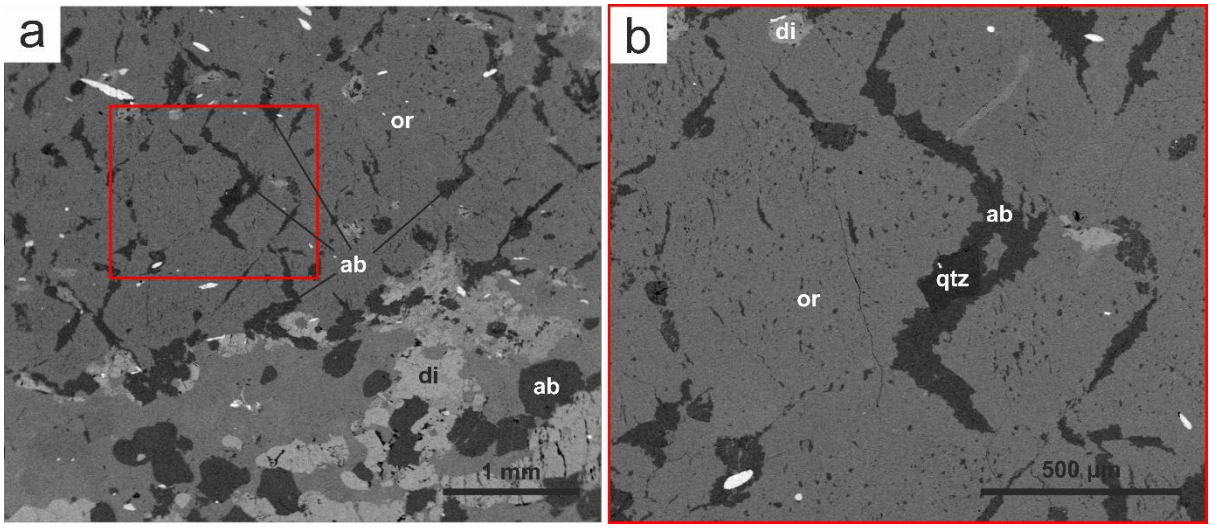

Fig. 23 BSE-Detail Images showing the *pinch* region of the pinch-and-swell structure of Type 2;
a) Transition zone between the marble and the aplite with a red rectangle defining the surroundings of b
b) Magnified image of the conjugated micro cracks filled by albite with a rare occurrence of quartz
Abbreviations stand for the following: albite (ab), orthoclase (or), diopside (di), quartz (qtz)

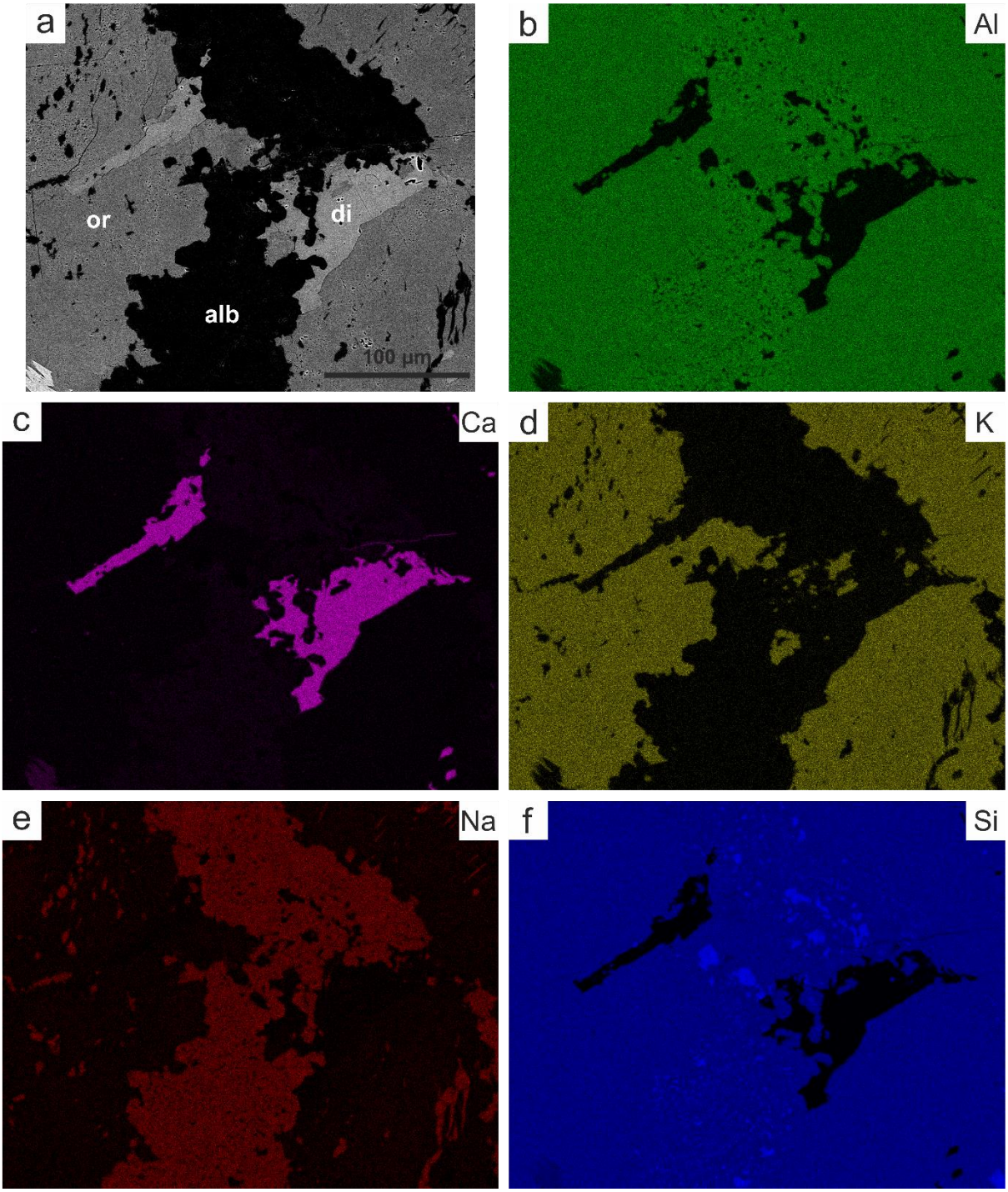

Fig. 24 BSE image of a micro crack inside the *pinch* zone and element distribution map featuring the elements (from a to f): Al, Ca, K, Na, Si.

Since the Rose Diagrams of Type 1 already showed varying orientations based on the location of the measured grains, the analysis for Type 2 should deliver more information regarding this aspect. The sample used for this analysis is the pinch-and-swell structure (Fig. 17 a). The Rose diagram for the *Host Rock* in Type 2 shows a rather random distribution of the SPO. Its direction is approximately NW-SE but looks very ambiguous. The *Rim* section of Type 2 is showing a very distinct orientation going approximately NW-SE (Fig. 25).

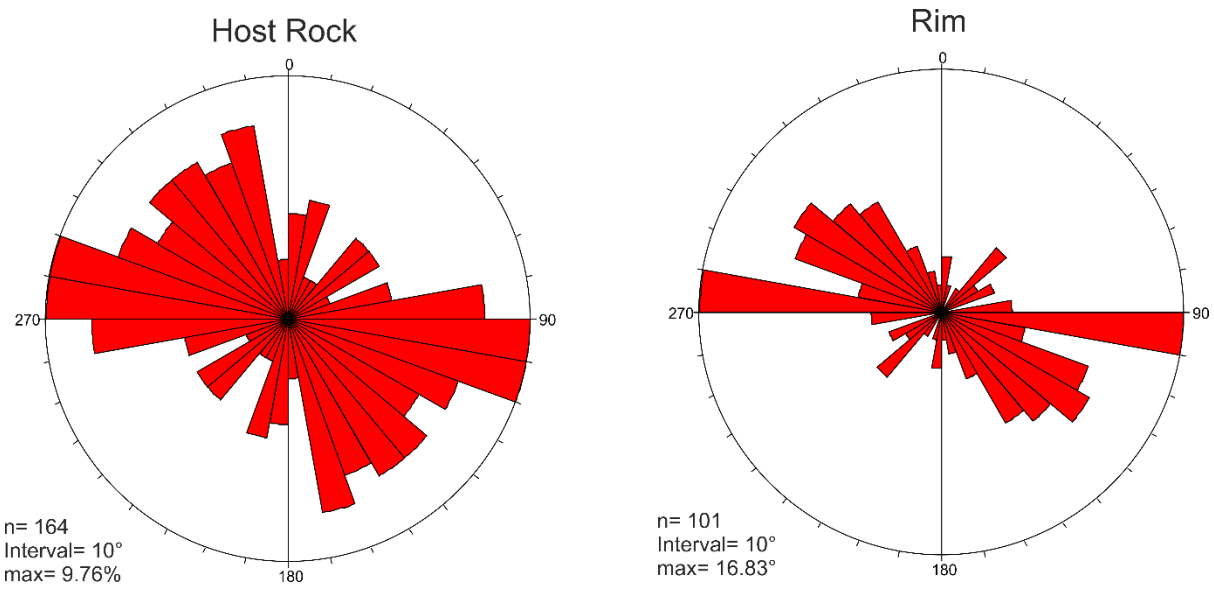

Fig. 25 Rose diagrams showing the 2D orientation of long axes of calcite grains in the *Host Rock*/*Rim* areas of sample a in Fig. 17.

The grainsize analysis in the form of two histograms representing the *Host Rock* and the *Rim* respectively show that with further distance to the dyke the amount of larger grains increases and smaller grains are more abundant in the vicinity of the aplite (Fig. 26). A total of 164 grains were analysed for the *Host Rock* and the histogram displays a rather equalized distribution of grainsize. However, more than 50% of the measured grains lie within the range of 60-240 µm and 80% of the grains don't have a higher grainsize than 420 µm. The remaining 20% are more or less evenly distributed over the larger grainsize classes (>420 µm). The two grainsize classes containing the most grains are 60 and 180 µm, containing 25 grains each but are closely followed by the classes representing similar sizes.

In the *Rim* section the grain distribution looks very much different, having a strong peak in the lowest grainsize class corresponding to 60 µm. Out of 101 measure grains 48 fall into the category of 60 µm which amounts to almost 50% of the total grains measured. After this class, the distribution curve makes a very sharp decline with almost 85% of measured grains lying within 240 µm. The remaining classes are barely represented, which stands in strong contrast to the distribution seen in the *Host Rock* section. Therefore, the *Host Rock* features a rather balanced distribution of grainsize, whereas the *Rim* mainly contains smaller grains.

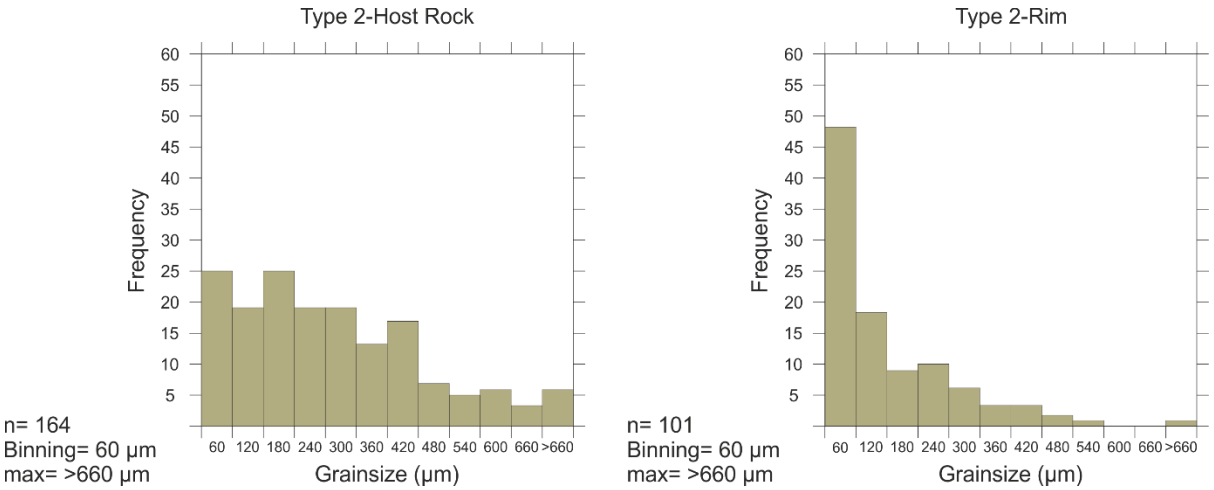

Fig. 26 Grainsize Histogram of the *Host Rock* section (left) and the *Rim* section (right) of sample a in Fig. 17

The EBSD results of Type 2 feature varying misorientation depending on the measured locality with the equivalent regions analysed as in Type 1 to receive comparable results (Fig. 27). The *Host Rock* only shows small amounts of average misorientation, ranging from 0-5° and with a maximum misorientation of 3.6° (Fig. 28 a). However, it features some low-angle grain boundaries, together with first evidence of deformation twinning. Looking at Misorientation Deviation of the area, there are only few zones of increased misorientation and one centre of high misorientation amounting to a value of 21° (Fig. 28 b). In the *Rim* the misorientation appears to be even lower than in the *Host Rock* with neither low-angle boundaries nor deformation twinning being present. The utmost amount of average misorientation measured in the section only totals to 2.3° (Fig. 28 c). When looked at the misorientation deviation of the *Rim* has a maximum of 15.2°, the lowest amount recorded during the EBSD analysis of these samples (Fig. 28 d). The *Rim* region therefore neither features a high average misorientation, nor a high heterogeneity. Although the misorientation deviation shows some areas that deviate from the general image, they form an exception. However, when looking at the *Core* region of the aplite, the internal misorientation inside the individual grains is highly amplified. There is a very high number of low-angle grain boundaries and Dauphiné-Twins. Additionally the grain boundaries themselves make a suturated appearance. Even though the average misorientation is rather low with an utmost value of 2.3° (Fig. 28 e), the heterogeneity inside the individual quartz grains is strongly enhanced. Due to high variance of misorientation deviation amounting to values of 19.8° (Fig. 28 f), the colour scheme that was chosen for the visualization of the misorientation is strongly shifting. This stands in strong contrast to the *Rim* section which barely features any misorientation.

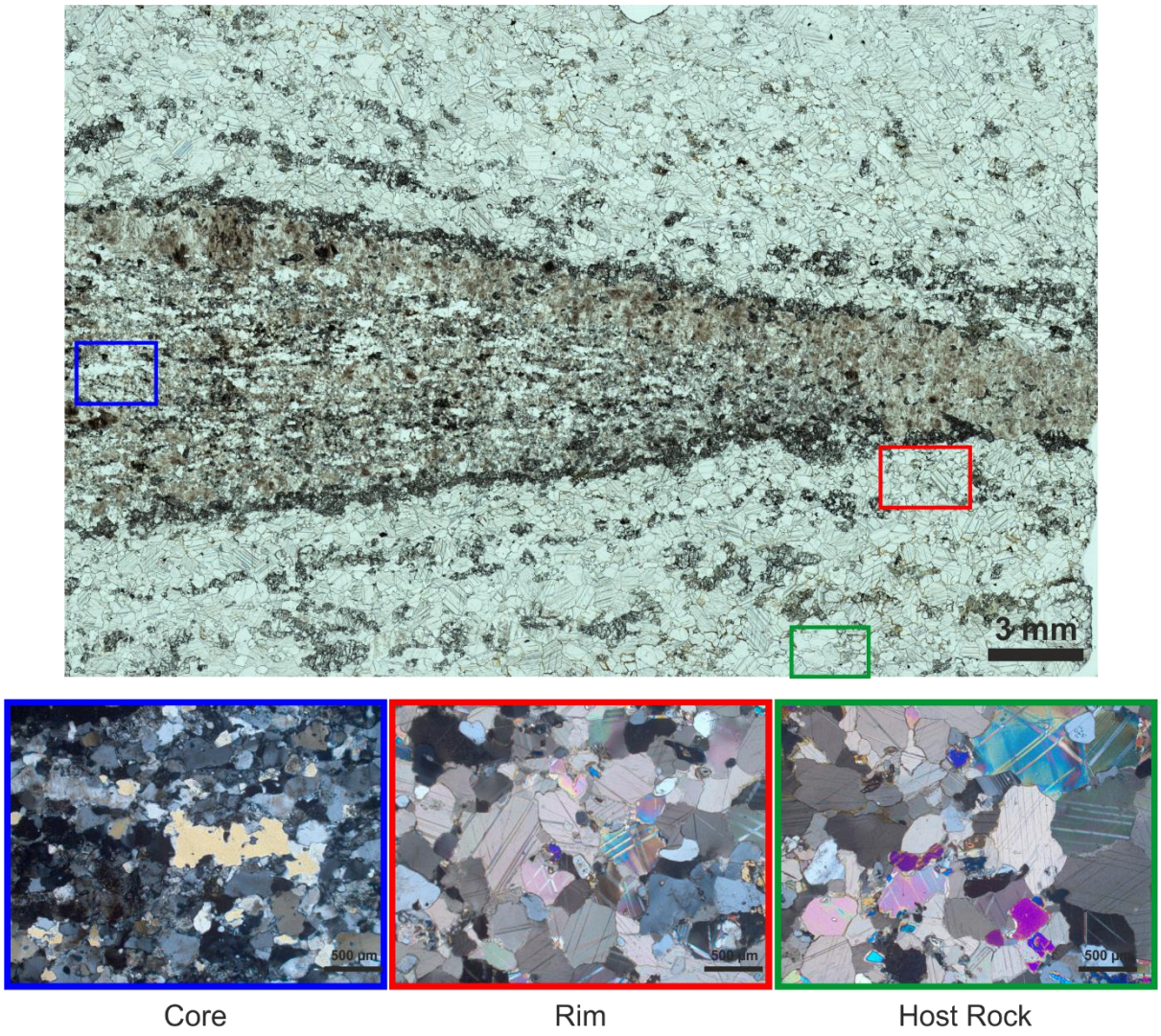

Fig. 27 Thin Section scan of sample a in Fig. 2 with three marked regions (coloured) symbolizing the sections analysed by EBSD.

Pole figures of calcite in the *Host Rock* show a weak preferred alignment of c-axis sup-parallel to the foliation and a similar preferred alignment of e poles even though in a more scattered manner. In the *Rim* region, the c-axis seems to be aligned along a broad girdle normal to the foliation while e-poles again display a similar preferred alignment but increasingly dispersed. (Fig. 29). Quartz grains within the *Core* seem to have a very weak CPO with the c axis being oriented along a foliation subparallel girdle (Fig. 29, Bestmann et al., 2006; Wilson et al., 2007).

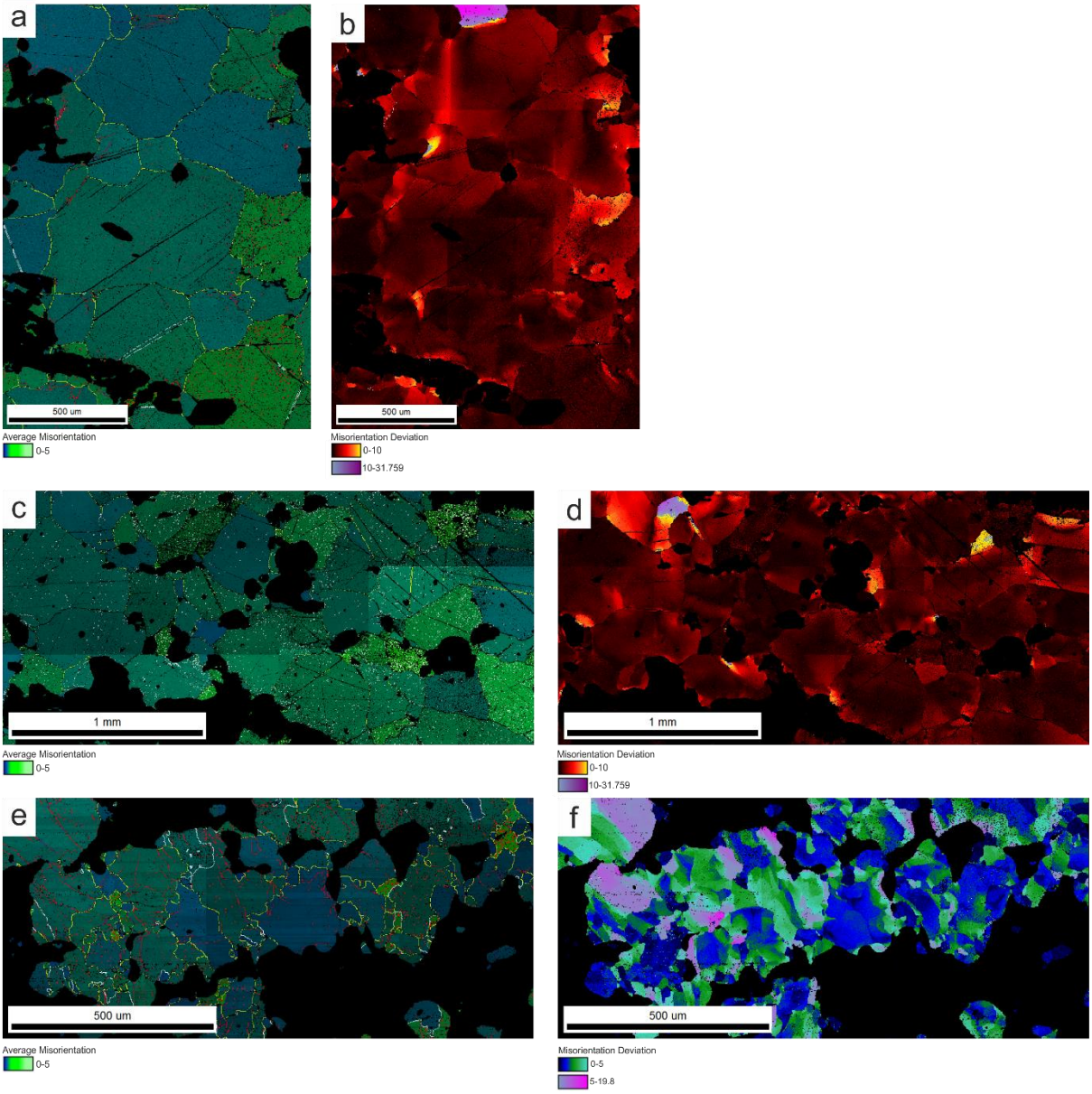

Fig. 28 Grain average misorientation and grain boundary map (left) and misorientation deviation angle map (right); Top to bottom: *Host Rock* (Cc), *Rim* (Cc), *Core* (Qtz); Grain Boundaries: 2-5° (red), 5-10° (violet), >10° (yellow), Twins (white); see text for detailed descriptions of a-f

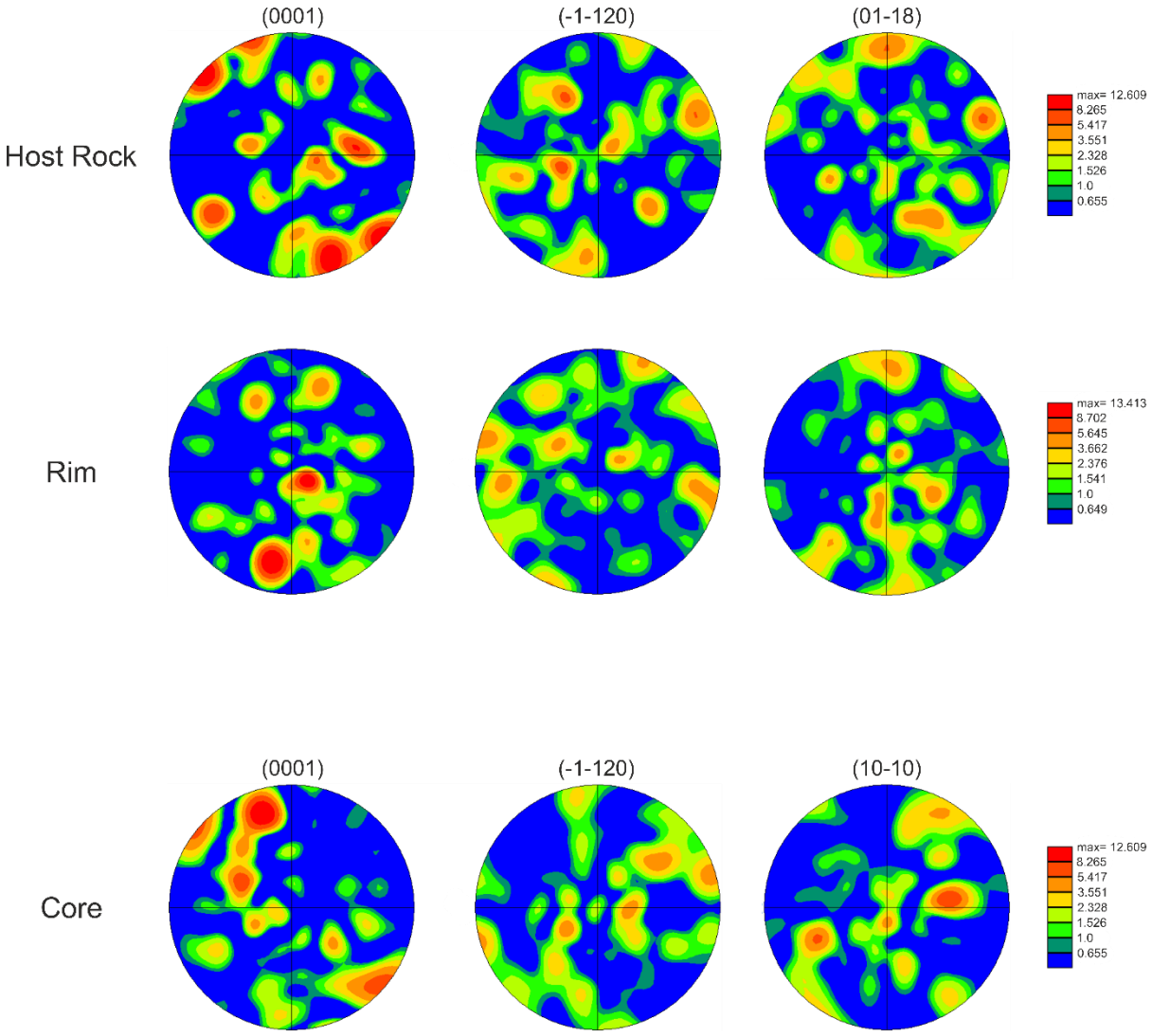

Fig. 29 Pole figures for the sections *Host Rock* (top), *Rim* (mid), *Core* (bottom) of Type 2 with their respective legends on the right; Analysed planes from left to right: Calcite: c, a, e; Quartz: c, a, m

The main points for Type 2-Pinch-and-Swell/Tapered Boudin include:

- Grain Size decreases with increasing proximity to the aplitic dyke
- Calcite grains show a similar SPO in the *Rim* and *Host rock* area
- Calcite grains show a similar average misorientation of up to xx° in the *Rim* and *Host Rock* area
- Quartz grains in the *Core* show a very high internal variation of misorientation in the individual grains
- The deformation seems to be concentrated in the internal regions of the aplitic dyke (Quartz)

Discussion

Boudinage Evolution in the Local Geodynamic Framework

The observed boudin structures within the outcrop document structures that can be related to an extensional (Fig. 5, left column) and a compressional regime, (Fig. 5, right column) though some samples even show evidence for both, compression and extension (Fig. 5, a). Cracks cross-cutting aplite dykes, blocky-domino boudins as well as pinch-and-swell structures (Fig. 5) are all indicative of an extensional stress regime (Lohest, 1909; Ramberg, 1955; Goscombe et al., 2004,). However, slight overlap of segments being pushed onto each other and folded boudin trails (Fig. 5 b, f) signify a follow-up compressional event (Dabrowski and Grasemann, 2014). The observation of these contradicting structures could be explained by a change in the local stress regime regarding orientation of σ1 and σ3 (Anderson 1905, 1951). Nevertheless, such a drastic change in the stress regime seems rather unlikely. Another possible explanation for the observed switch from extensional to compressional structures could be the rotation of intruded dykes into different fields of instantaneous stretching/shortening and the consequential varying behavior of these dykes (Fossen, 2016). Considering the fact, that all other structures observed in the quarry are consistent with constant top to the south shearing (Poisel et al., 2016) the latter theory is the favoured one. The different steps of from the dykes intruding, getting rotated and/or boudinaged depending on their orientation is illustrated in a conceptual model (Fig. 30).

After Goscombe and Passchier (2003), assymetric boudinage can be utilized to deduct shear sense indicators with the help of a fabric attractor. In comparison to deformation fabrics boudinage hardly gets completely removed from the rock record and survives multiple deformation events (Goscombe et al., 2004). Even though it isn't possible to deduct a shear sense from the samples taken, there are signs of successive deformation episodes in the form of chaotic boudin assemblages (Fig. 5 f). This boudin type is classified by Goscombe et al., (2004) as a *reworked* boudin, modified by subsequent deformational episodes. After the original separation of the aplite into boudin segments, the individual blocks were whirled around in the host rock matrix, whereby their rotation rate drastically increased after the upper corner of a segment reached the lower corner of the neighbouring segment (Dabrowski and Grasemann, 2014). The whole assemblage then was overprinted by folding, marking a compressional component that is observed in other samples as well. This behaviour is usually restricted to thin aplitic layers of a couple mm thickness that fold due to their aspect ratio (Fig. 5 b), but can also occur in a larger scale where the boudin segments reach a thickness of couple cm (Fig. 5 f; Dabrowski and Grasemann, 2014) . The prior signs for a switch of extension to compression could be the result of the migration of material lines into different sectors (Fossen, 2016) but the chaotic assemblage and holistic folding of the boudin segments is difficult explain with this hypothesis.

After Dabrowski and Grasemann, (2014) a high aspect ratio and a greater width of the inter-boudin zone facilitate a strong increase in rotation rate, which would explain the strong dispersal of the boudin segments seen in the sample (Fig. 5 b). Modelling done by Dabrowski and Grasemann, (2014) shows that with increasing shear strain boudin trains become increasingly turbulent, meaning the area was at least temporarily affected by high shear strains (γ = >20). This assumption is supported by domino boudinage (Hanmer and Passchier, 1991) often being a qualitative indicator for high shear strain (Fig. 5 a, b; Dabrowski, and Grasemann, 2014)

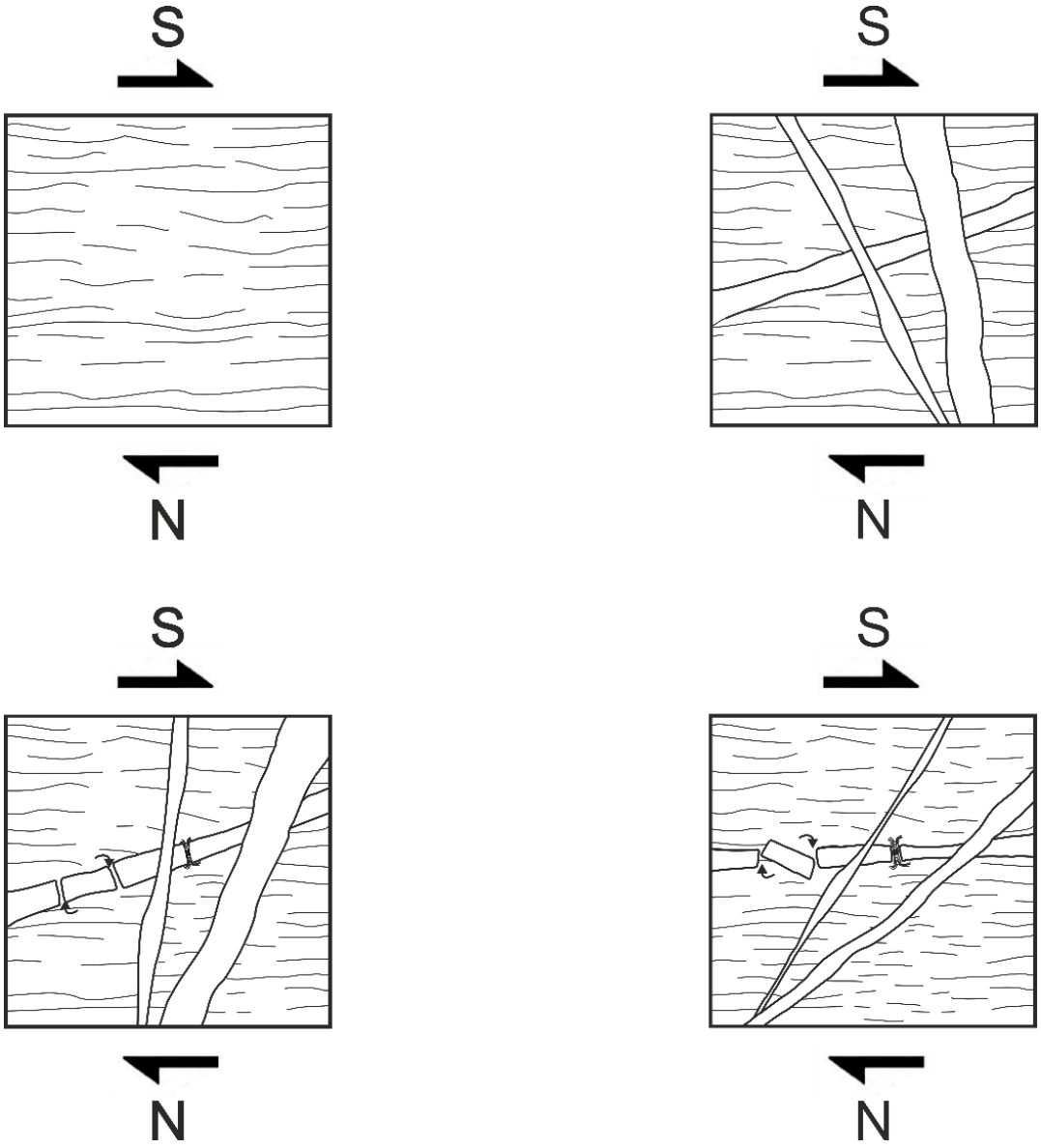

Fig. 30 Geodynamic model attempting to visualize the continuous processes in four images each depicting a certain stage as follows (from upper left to bottom right):

1. Relatively undisturbed marble host rock with horizontal, subparallel foliation
2. Intrusion of the pegmatitic and aplitic dykes with varying orientation
3. Depending on the initial orientation of the dykes top-to-the-SE shearing causes rotation, stretching and shortening of the dykes
4. After thinning and separating of boudins, individual segments start to rotate. Local shortening may cause folding and tiling of rotated segments.

Deformation-Induced Reactions

Even though no quantitative geochemical analysis via electron microprobe has been performed, some petrological observations made by optical microscopy and SEM should be discussed as they might help to clarify temperature constraints. Regarding the evaluation of microscopical analysis, the prominent diopside seam around the intruded dykes might be the product of a metasomatic reaction between calcite ($CaCO_3$) and migrating quartz (SiO_2) of the aplite (Hover Granath et al., 1983; Labotka et al., 1988; Ferry and Dipple, 1992). The diopside seam is always situated along the transition of the marble host rock into the aplite and appears along blocky-domino boudins (Type 1) as well as pinch-and-swell structures (Type 2). However, this seam is not present in inter-boudin zones indicating it was formed prior to the brittle fractures seen in the Type 1 Boudins (Fig. 6). Albite shows a similar behaviour as diopside in the way that it also appears in high concentrations around the transition zones of the aplite and the marble (purple in the phase maps). For the diopside reaction to develop, the mobilization of quartz is critical. This migration could be enabled by pressure solution transporting the quartz from the inner aplite to the outer rims (Robin, 1978; Wheeler, 1987a, 1992; Knipe, 1989). This process is especially proncounced in the pinch-and-swell structure featuring two areas only millimeters apart, one containing quartz (right), the other being virtually devoid of it (left) (Fig. 18, yellow arrows and Fig. 21, 22). This might be due to the quartz being transported from zones of high strain to localities of relatively lower strain like internal cracks or inter-boudin zones, both being caused by aforementioned extension (Lohest, 1909; Ramberg, 1955; Goscombe et al., 2004,). Furthermore, most of the aplitic dykes are depleted of quartz at their lithological transitions into the marble (Fig. 10, 21 and 22), which could be due to the metasomatic reactions occuring at these zones.
Within high-strain areas, the exsolution of perthite grains and lamellae is highly amplified, showing that deformation enhances metamorphic reaction (Chapman et al., 2019). It appears that inside these high-strain zones, exsolution is mainly facilitated via brittle precursors in the form of conjugated micro cracks (Fig. 22).

Active Deformation Mechanisms

Due to the variety of boudin structures met at the site of investigation, one of the main goals of this thesis was to analyse the active deformation mechanisms. In order to properly comprehend this variation, it was not only important to understand the mechanisms that led to these structures, but also when and to what degree they were active and how they transitioned into each other depending on the conditions during deformation. One important deformation mechanism that can be traced throughout the rock record is dissolution-precipitation in the form of quartz being solved, transported and precipitating or reacting to different minerals at zones of comparatively lower strain (Robin, 1978; Wheeler 1987a, 1992; Knipe 1989; Passchier and Trouw, 2005). Crucial examples for these areas are lithological transitions between the aplite and the marble or inter-boudin zones. Besides of quartz, other

minerals like chlorite can likewise precipitate in these areas and record deformation as seen in the chlorite forming kink bands (Williams and Price, 1990; Pryer, 1993; Ji, 1998 a, b; Nishikawa and Takeshita, 1999). These kink bands are evidence for a continuation of deformation after the growth of the chlorite. However, although kinking is not strictly limited to certain crystallographic planes and directions as it is the case for deformation twinning, it is only able to accommodate lower amounts of strain (Passchier and Trouw, 2005).

The orientation of the grains in the Rose diagrams show an SPO, which reveals information on how the grains could have been rotated during the deformation when the *Host Rock* is compared with the *Rim* section. In Type 1 the *Host Rock* has a rather distinct SPO going approximately E-W. This could be due to it being sufficiently affected by the deformation for the calcite grains to form an SPO. The *Rim* zone of Type 1 shows a slightly different trend with a more vergent orientation. This variance might be due to passive rotation of the individual grains (Passchier and Trouw, 2005). It stands to reason that during the rotation and deformation of the dykes the surrounding grains were affected by this rotation in a comparatively stronger manner due to their proximity and therefore were rotated mutually together with the dykes. However, the results of the Rose diagrams in Type 2 neither confirm nor support this idea. Here, the orientation of the grains in the *Host Rock* seems much more random and is going approximately NW-SE. This could have its reason in how this sample was deformed. Perhaps the slower, more continuous deformation that lead to this pinch-and-swell structure allowed a greater portion of the grains to be realigned accordingly, compared to the more rapid fracturing that occurs in Type 1. The *Rim* region of Type 2 is again very similar to what was seen in Type 1, meaning deformation seems to be localized. The histograms contrasting the grainsize of these two regions, again for Type 1 and 2, should reinforce the idea of a smaller grainsize in the vicinity of dykes. This would also concur with the idea of localized deformation, it being highest on the zones of lithological transition. Even though the results of Type 1 show that there seem to be more larger grains in the *Host Rock* area than in the *Rim*, a clear assertion on this matter can not be made. Type 2 gives a much more unambiguous impression with the *Host Rock* having a great abundance of larger grains relative to the finer grained *Rim*. This reduction of the grainsize can be understood as a result of the heterogeneity of the deformation concentration throughout the rock mass and might be closely related to the rotation of the dykes after their intrusion and subjection to the preexisting top-to-the SE paleostress field (Poisel et al., 2016; Racek et al., 2017). The calcite grains situated closer to the mostly aplitic dykes were affected by this rotation to a greater degree compared to grains located further away. Since deformation seems localised and centered aroud the aplitic rims, recrystallisation mechanisms in the form of Subgrain Rotation (SGR) (White, 1976; Poirier and Guillopé, 1979; Urai et al., 1986; Halfpenny et al., 2006) could represent one of the factors leading to a smaller grainsize. Due to the heterogeneity of mineralogic composition along the rims of the aplites, mineral pinning might act as another plausible cause for this decrease in grainsize, since the grains of these minerals (e.g. calcite, diopside, albite) could inhibit each others growth (Herwegh et al., 2011). The marble host rock experienced lower amounts of deformation due to it being further away from the litholigical

transition representing the centre of deformation due to rheological differences (Pennacchioni and Mancktelow, 2018).

The EBSD-Results indicate a low amount of Misorientation in the *Host Rock* region in Type 1 as well as Type 2, which seems plausible when considered that deformation is localized around the transition between the marble host rock and the aplite, or the aplite itself. The *Rim* sections are different in that Type 1 seems to accommodate a comparatively higher amount of strain in this region, whereas Type 2 still only features low misorientation. Thus, it must be the case that the deformation in Type 2 is concentrated in the *Core* region. When looked at the *Core*, it reveals that it harbors the main portion of deformation and that it is localized in this area. The high abundancy of subgrains boundaries in this area together with the suturated grain boundaries further indicate that recrystallisation mechanisms like Grain Boundary Migration (GBM) (Poirier and Guillopé, 1979; Urai et al., 1986; Stipp et al., 2002) and SGR (White, 1976; Poirier and Guillopé, 1979; Urai et al., 1986; Halfpenny et al., 2006) were active. This stands in strong contrast to Type 1 where the *Core* merely shows a couple of smaller zones with a higher misorientation and the *Rim* being the region to have accomodated the highest amounts of deformation. The results of the Pole figures which were done for Type 1 and Type 2 respectively, show first trends of preferred alignments mainly along the c axes but the limited amont of results don't allow for further deductions.

Different deformation mechanisms were active in the two End-Members which were compared and deformation localizes at certain areas indicating these structures might have been formed at different conditions and therefore times. This is in agreement with the prominent diopside rims being present around pinch-and-swell structures but not brittle cracks that were formed at a later stage.
Considering all of the abovementioned factors including the drawn conceptual model, the following geodynamic history can be established: Aplitic and rarely pegmatitic dykes intruded into a impure marble host rock containing scattered portions of diopside. These dykes were subjected to a preexisting top-to-the-SE paleostress field by which they were stretched, rotated and boudinaged depending on their orientation (Poisel et al., 2016, Goscombe et al., 2004). The occurring pinch-and-swell structures deforming continuously indicate temperatures of at least ~500 C° due to the ductile behaviour of feldspar (Fossen 2016). Furthermore the high abundance of diopside points towards temperatures between 475 and 600 C° (Hover Granath et al., 1983). During the generation of these pinch-and-swell structures, quartz migrated via pressure solution from zones of high-strain (*pinch*) to zones of relatively lower strain (*Rim*) (Robin, 1978; Wheeler 1987a, 1992; Knipe 1989; Passchier and Trouw, 2005). At these zones of lithological transition the quartz could have reacted together with the calcite and generated a younger generation of diopside formed as a seam around the aplites (Hover Granath et al., 1983; Labotka et al., 1988; Ferry and Dipple, 1992). In comparison to the Type 1 End-Members, which do not show signs of a diopside seam along their inter-boudin zones, this seam appears in the inter-boudin zones of pinch-and-swell

structures (Type 2), further indicating these structures were formed at an earlier, i.e. warmer stage. This episode of ductile deformation with high temperatures (> 500 C°) was the time were crystalplastic behaviour dominated in the form of dislocation glide and creep (Hull and Bacon, 2001; Poirier, 1985; Tullis and Yund, 1991). In addition to these deformation mechanisms, pressure solution and recrystallisation mechanisms like GBM and SGR were active to accommodate larger strains together with deformation twins and kink bands which both are only capable of accomodating limited amounts of strain (Passchier and Trouw, 2005). After the continuous cooling of the area, there was a shift in boudinage types from continuous deformation (Type 2) to brittle structures (Type 1). During this period of brittle deformation cracks acting as zones of relatively lower strain were formed that later were filled by precipitations of minerals like quartz or chlorite (Robin, 1978; Wheeler 1987a, 1992; Knipe 1989; Passchier and Trouw, 2005), which recorded the still ongoing deformation in the form of kink bands (Williams and Price, 1990; Pryer, 1993; Ji, 1998a, b; Nishikawa and Takeshita, 1999).

Outlook

Considering the abovementioned aspects, the structural complexity of the area is not only apparent via the variability of boudin structures but likewise can be witnessed in individual samples that lead to different conclusions. The original goal of identifying the active deformation mechanisms and investigating when and why they were active was achieved by a microfabrics analysis, although only partially. The created geodynamic model (Fig. 30) explains the situation encountered at the quarry Fehringer well and is in accordance with past studies done by Dabrowski and Grasemann (2014). Furthermore, the comparison of the two End-Member boudin types revealed that deformation is localized and their divergence in behaviour could be due to these structures being formed under different conditions and therefore times. However, to bring more light into these complex issues a greater dataset covering more samples regarding grainsize, orientation and shape analysis would be necessary. A representative amount of additional samples would need to be analysed under the SEM and the EBSD detector to receive more information on the localisation of deformation, the latter representing one of the most important results of this project. Especially the internal deformation in certain areas is of particular interest. However, the capacities necessary to conduct these measures are beyond the limits of this project and are therefore a matter of the future.

Conclusions

The main conclusion that can be drawn from the project are the following:

- The grainsize and SPO analysis both show that deformation was heterogenous and that it is localised, with a focus on either the *Rim* or the *Core*. Histograms evaluating the grainsize further document a reduction in grains with increasing proximity towards the aplite.

- Minerals like quartz can migrate via pressure solution to zones of lesser strain, like inter-boudin-zones or internal cracks. There they can precipitate again and form quartz wedges or perhaps constitute chemical components for reactions, for example: Calcite ($CaCO_3$) + Quartz(SiO_2) + Mg (derived from preexisting diopside in the marble) => Diopside ($CaMgSi_2O_6$).

- Multiple samples document a change of paleostress directions, with extension occuring prior to a follow-up compressional event. However, this might also be explained via the dykes being rotated in different fields of instantaneous stretching/shortening and therefore reacting in this manner. In fact, this explanation seems more plausible than such a drastic change in the orientation of σ1/σ3.

- The most important factors influencing the great variety of boudin types seem to include aspect ratio and the original orientation of the intruded dykes with respect to the paleo stress-field.

Table of Figures

References

Abart, R., Heuser, D., & Habler, G. (2014). Mechanisms of myrmekite formation: case study from the Weinsberg granite, Moldanubian zone, Upper Austria. Contributions to Mineralogy and Petrology, 168(5), 1074.

Anderson, E., M. (1905). The dynamics of faulting. Transactions of the Edinburgh Geological Society, 8(3), 387-402.

Anderson E., M. (1951) The Dynamics of Faulting, 2nd edn. Edinburgh, UK: Oliver and Boyd.

Bestmann, M., Prior, D. J., & Grasemann, B. (2006). Characterisation of deformation and flow mechanics around porphyroclasts in a calcite marble ultramylonite by means of EBSD analysis. Tectonophysics, 413(3-4), 185-200.

Carreras, J., Cosgrove, J. W., & Druguet, E. (2013). Strain partitioning in banded and/or anisotropic rocks: Implications for inferring tectonic regimes. Journal of Structural Geology, 50, 7-21.

Chapman, T., Clarke, G. L., Piazolo, S., & Daczko, N. R. (2019). Inefficient high-temperature metamorphism in orthogneiss. American Mineralogist: Journal of Earth and Planetary Materials, 104(1), 17-30.

Cooke, R. A. (2000). High-pressure/temperature metamorphism in the St. Leonhard Granulite Massif, Austria: evidence from intermediate pyroxene-bearing granulites. International Journal of Earth Sciences, 89(3), 631-651.

Dabrowski, M., & Grasemann, B. (2014). Domino boudinage under layer-parallel simple shear. Journal of Structural Geology, 68, 58-65.

Dudek, A. (1980). The crystalline basement block of the Outer Carpathians in Moravia: BrunoVistulicum. Rozpr. Cs. Akad. Ved, R. mat. prir. ved, Praha, 90, 1-85.

Ferry, J. M., & Dipple, G. M. (1992). Models for coupled fluid flow, mineral reaction, and isotopic alteration during contact metamorphism: The Notch Peak aureole, Utah. American Mineralogist, 77(5-6), 577-591.

Fiala, J. (1987). Moldanubian granulites: source material and petrogenetic considerations. Neues Jahrbuch fur Mineralogie Abhandlungen, 157, 133-165.

Finger, F. (2003). U-Pb shrimp dating and trace element investigations on multiple zoned zircons from a South-Bohemian granulite. Journal of Geosciences, 48(1-2), 51-0.

Fossen, H. (2016). Structural geology. Cambridge University Press.

Fuchs, G., & Matura, A. (1976). Zur Geologie des Kristallins der Böhmischen Masse. Jb. Geol. B. A, 119(1), 1-43.

Goldstein, A. G. (1988). Factors affecting the kinematic interpretation of asymmetric boudinage in shear zones. Journal of Structural Geology, 10(7), 707-715.

Goscombe, B. D., & Passchier, C. W. (2003). Asymmetric boudins as shear sense indicators—an assessment from field data. Journal of Structural Geology, 25(4), 575-589.

Goscombe, B. D., Passchier, C. W., & Hand, M. (2004). Boudinage classification: end-member boudin types and modified boudin structures. Journal of Structural Geology, 26(4), 739-763.

Grasemann, B., & Stüwe, K. (2001). The development of flanking folds during simple shear and their use as kinematic indicators. Journal of Structural Geology, 23(4), 715-724.

Halfpenny, A., Prior, D. J., & Wheeler, J. (2006). Analysis of dynamic recrystallization and nucleation in a quartzite mylonite. Tectonophysics, 427(1-4), 3-14.

Hanmer, S. (1991). Shear-sense indicators: a review. Geol. Surv. Canada Pap., 90, 1-71.

Hasalová, P., Schulmann, K., Lexa, O., Štípská, P., Hrouda, F., Ulrich, S., ... & Týcová, P.

(2008). Origin of migmatites by deformation-enhanced melt infiltration of orthogneiss: A new model based on quantitative microstructural analysis. Journal of Metamorphic Geology, 26(1), 29-53.
Heilbronner, R., & Barrett, S. (2013). Image analysis in earth sciences: microstructures and textures of earth materials (Vol. 129). Springer Science & Business Media.
Herwegh, M., Linckens, J., Ebert, A., Berger, A., & Brodhag, S. H. (2011). The role of second phases for controlling microstructural evolution in polymineralic rocks: A review. Journal of Structural Geology, 33(12), 1728-1750.
Hobbs, B.E., Means, W.D., Williams, P.F., 1976. An Outline of Structural Geology. John Wiley and Sons, 278–280.
Hover Granath, V. C., Papike, J. J., & Labotka, T. C. (1983). The Notch Peak contact metamorphic aureole, Utah: Petrology of the Big Horse limestone member of the Orr Formation. Geological Society of America Bulletin, 94(7), 889-906.
Hull, D., & Bacon, D. J. (2001). Introduction to dislocations. Butterworth-Heinemann.
Iyer, K., & Podladchikov, Y. Y. (2009). Transformation-induced jointing as a gauge for interfacial slip and rock strength. Earth and Planetary Science Letters, 280(1-4), 159-166.
Janoušek, V., Finger, F., Roberts, M., Frýda, J., Pin, C., & Dolejš, D. (2004). Deciphering the petrogenesis of deeply buried granites: whole-rock geochemical constraints on the origin of largely undepleted felsic granulites from the Moldanubian Zone of the Bohemian Massif. Earth and Environmental Science Transactions of The Royal Society of Edinburgh, 95(1-2), 141-159.
Ji, S. (1998a) Deformation microstructure of natural plagioclase. In: Snoke, A., Tullis, J., Todd V., R. (eds) Fault related rocks – a photographic atlas. Princeton University Press, New Jersey, pp 276–277
Ji, S. (1998b) Kink bands and recrystallization in plagioclase. In: Snoke, A., Tullis, J., Todd, V., R. (eds) Fault related rocks – a photographic atlas. Princeton University Press, New Jersey, pp 278–279
Jordan, P. G. (1991). Development of asymmetric shale pull-aparts in evaporite shear zones. Journal of Structural Geology, 13(4), 399-409.
Kidan, T. W., & Cosgrove, J. W. (1996). The deformation of multilayers by layer-normal compression; an experimental investigation. Journal of Structural Geology, 18(4), 461-474.
Klein, C., & Philpotts, A. R. (2013). Earth materials: introduction to mineralogy and petrology. Cambridge University Press.
Knipe, R. J. (1989). Deformation mechanisms—recognition from natural tectonites. Journal of Structural Geology, 11(1-2), 127-146.
Kolenovská, E., Schulmann, K., Klápová, H., & Štıpská, P. (1999). Tectonometamorphic evolution of the Moldanubian zone near Jemnice (south Moravia, Bohemian Massif). Beih Eur J Mineral, 11, 91-94.
Kröner, A., Wendt, I., Liew, T. C., Compston, W., Todt, W., Fiala, J., ... & Vanek, J. (1988). U-Pb zircon and Sm-Nd model ages of high-grade Moldanubian metasediments, Bohemian Massif, Czechoslovakia. Contributions to Mineralogy and Petrology, 99(2), 257-266.
Kröner, A., O'Brien, P. J., Nemchin, A. A., & Pidgeon, R. T. (2000). Zircon ages for high

pressure granulites from South Bohemia, Czech Republic, and their connection to Carboniferous high temperature processes. Contributions to Mineralogy and Petrology, 138(2), 127-142.
Labotka, T. C., Nabelek, P. I., & Papike, J. J. (1988). Fluid infiltration through the Big Horse Limestone Member in the Notch Peak contact-metamorphic aureole, Utah. American Mineralogist, 73(11-12), 1302-1324.
Linner, M. (1996). Metamorphism and partial melting of paragneisses of the Monotonous Group, SE Moldanubicum (Austria). Mineralogy and Petrology, 58(3-4), 215-234.
Linner, M (2013). Metamorphoseentwicklung und Deckenbau des Moldanubikums mit Fokus auf den Raum Melk – Dunkelsteinerwald. Arbeitstagung der Geologischen Bundesanstalt 2013 – Melk, Vorträge
Lohest, M. (1909). De l'origine des veines et des ge'odes des terrains primaires de Belgique. Ann. Soc. Geol. Belgique., 36, B275-282.
Mandal, N., Dhar, R., Misra, S., & Chakraborty, C. (2007). Use of boudinaged rigid objects as a strain gauge: Insights from analogue and numerical models. Journal of structural geology, 29(5), 759-773.
Marques, F. O., Fonseca, P. D., Lechmann, S., Burg, J. P., Marques, A. S., Andrade, A. J., & Alves, C. (2012). Boudinage in nature and experiment. Tectonophysics, 526, 88-96.
Matura, A. (1989). Erläuterungen zu Blatt 37 Mautern (mit Beiträgen von Heinz, H.). Geologische Bundesanstalt.
Medaris Jr, G., Jelínek, E., & Mísař, Z. (1995). Czech eclogites: Terrane settings and implications for Variscan tectonic evolution. Eur. J. Mineral, 7, 7-28.
Nahodilová, R., Štípská, P., Powell, R., Košler, J., & Racek, M. (2014). High-Ti muscovite as a prograde relict in high pressure granulites with metamorphic Devonian zircon ages (Běstvina granulite body, Bohemian Massif): consequences for the relamination model of subducted crust. Gondwana Research, 25(2), 630-648.
Nishikawa, O., & Takeshita, T. (1999). Dynamic analysis and two types of kink bands in quartz veins deformed under subgreenschist conditions. Tectonophysics, 301(1-2), 21-34.
O'Brien, P. J. (1997). Garnet zoning and reaction textures in overprinted eclogites, Bohemian Massif, European Variscides: a record of their thermal history during exhumation. Lithos, 41(1-3), 119-133.
Passchier, C. W., & Druguet, E. (2002). Numerical modelling of asymmetric boudinage. Journal of Structural Geology, 24(11), 1789-1803.
Passchier, C. W., & Trouw, R. A. (2005). Microtectonics. Springer Science & Business Media.
Pennacchioni, G., & Mancktelow, N. S. (2018). Small-scale ductile shear zones: neither extending, nor thickening, nor narrowing. Earth-Science Reviews.
Petrakakis, K. (1997). Evolution of Moldanubian rocks in Austria: review and synthesis. Journal of Metamorphic Geology, 15(2), 203-222.
Poirier, J. P. (1985). Creep of crystals: high-temperature deformation processes in metals, ceramics and minerals. Cambridge University Press.
Poirier, J. P., & Guillopé, M. (1979). Deformation induced recrystallization of minerals. Bulletin de Mineralogie, 102(2), 67-74.
Poisel, R., Kolenprat, B., Bertagnoli, M., Ahmadabadi, M., Grasemann, B., & Hödlmoser, N. (2016). The rockslide hazard in the former quarry near Spitz and its foreland/Die Felssturzgefahr im ehemaligen Tagebau Spitz ad Donau und dessen Vorland. Geomechanics and Tunnelling, 9(5), 497-507.

Pryer, L. L. (1993). Microstructures in feldspars from a major crustal thrust zone: the Grenville Front, Ontario, Canada. Journal of structural Geology, 15(1), 21-36.
Racek, M., Lexa, O., Schulmann, K., Corsini, M., Štípská, P., & Maierová, P. (2017). Re-evaluation of polyphase kinematic and 40 Ar/39 Ar cooling history of Moldanubian hot nappe at the eastern margin of the Bohemian Massif. International Journal of Earth Sciences, 106(2), 397-420.
Racek, M., Štípská, P., Pitra, P., Schulmann, K., & Lexa, O. (2006). Metamorphic record of burial and exhumation of orogenic lower and middle crust: a new tectonothermal model for the Drosendorf window (Bohemian Massif, Austria). Mineralogy and Petrology, 86(3-4), 221-251.
Racek, M., Štípská, P., & Powell, R. (2008). Garnet–clinopyroxene intermediate granulites in the St. Leonhard massif of the Bohemian Massif: ultrahigh-temperature metamorphism at high pressure or not?. Journal of Metamorphic Geology, 26(2), 253-271.
Ramberg, H. (1955). Natural and experimental boudinage and pinch-and-swell structures. The Journal of Geology, 63(6), 512-526.
Ramsay, A.C., 1881. The Geology of North Wales. Memoirs of the Geological Survey of Great Britain, 3.
Robin, P. Y. F. (1978). Pressure solution at grain-to-grain contacts. Geochimica et Cosmochimica Acta, 42(9), 1383-1389.
Schmalholz, S. M., Schmid, D. W., & Fletcher, R. C. (2008). Evolution of pinch-and-swell structures in a power-law layer. Journal of Structural Geology, 30(5), 649-663.
Sederholm, J. J. (1899). Uber eine Archaische Sediment formation im Südwestlichen Finland und ihre Bedeutung...
Stipp, M., Stünitz, H., Heilbronner, R., & Schmid, S. M. (2002). The eastern Tonale fault zone: a 'natural laboratory'for crystal plastic deformation of quartz over a temperature range from 250 to 700 C. Journal of Structural Geology, 24(12), 1861-1884.
Štípská, P., & Powell, R. (2005). Does ternary feldspar constrain the metamorphic conditions of high-grade meta-igneous rocks? Evidence from orthopyroxene granulites, Bohemian Massif. Journal of Metamorphic Geology, 23(8), 627-647.
Štípská, P., Schulmann, K., & Powell, R. (2008). Contrasting metamorphic histories of lenses of high-pressure rocks and host migmatites with a flat orogenic fabric (Bohemian Massif, Czech Republic): a result of tectonic mixing within horizontal crustal flow?. Journal of Metamorphic Geology, 26(6), 623-646.
Swanson, M. T. (1992). Late Acadian-Alleghenian transpressional deformation: evidence from asymmetric boudinage in the Casco Bay area, coastal Maine. Journal of Structural Geology, 14(3), 323-341.
Tajčmanová, L., Konopásek, J., & Schulmann, K. (2006). Thermal evolution of the orogenic lower crust during exhumation within a thickened Moldanubian root of the Variscan belt of Central Europe. Journal of Metamorphic Geology, 24(2), 119-134.
Thiele, O. (1976). Zur Tektonik des Waldviertels in Niederösterreich (südliche Böhmische Masse). Nova Acta Leopoldina, 45, 67-82.
Tullis, J., & Yund, R. A. (1991). Diffusion creep in feldspar aggregates: experimental evidence. Journal of Structural Geology, 13(9), 987-1000.
Urai, J., Means, W.D., Lister, G.S., (1986) Dynamic recrystallization of minerals. In: Heard, H.C., Hobbs, B.E., (eds) Mineral and rock deformation: laboratory studies, the Paterson volume. Geophys Monogr 36:161–200, Am Geophys Union, Washington DC

Wheeler, J. (1987). The significance of grain-scale stresses in the kinetics of metamorphism. Contributions to Mineralogy and Petrology, 97(3), 397-404.
Wheeler, J. (1992). Importance of pressure solution and Coble creep in the deformation of polymineralic rocks. Journal of Geophysical Research: Solid Earth, 97(B4), 4579-4586.
White, S. H. (1976). The role of dislocation processes during tectonic deformation with special reference to quartz. The physics and chemistry of minerals and rocks, 75-91.
Williams, P. F., & Price, G. P. (1990). Origin of kinkbands and shear-band cleavage in shear zones: an experimental study. Journal of Structural Geology, 12(2), 145-164.
Wilson, C. J., RUSSELL-HEAD, D. S., Kunze, K., & Viola, G. (2007). The analysis of quartz c-axis fabrics using a modified optical microscope. Journal of Microscopy, 227(1), 30-41.
Yund, R. A., & Tullis, J. (1991). Compositional changes of minerals associated with dynamic recrystallizatin. Contributions to Mineralogy and Petrology, 108(3), 346-355.
Zeitlhofer, H., Schneider, D., Grasemann, B., Petrakakis, K., & Thöni, M. (2014). Polyphase tectonics and late Variscan extension in Austria (Moldanubian Zone, Strudengau area). International Journal of Earth Sciences, 103(1), 83-102.